

Bond Additivity and Persistent Geometric Imprints of Entanglement in Quantum Thermalization

Chun-Yue Zhang,^{1,2} Shi-Xin Zhang,^{1,*} and Zi-Xiang Li^{1,2,†}

¹*Beijing National Laboratory for Condensed Matter Physics & Institute of Physics, Chinese Academy of Sciences, Beijing 100190, China*

²*University of Chinese Academy of Sciences, Beijing 100049, China*

(Dated: January 6, 2026)

Characterizing the intricate structure of entanglement in quantum many-body systems remains a central challenge, as standard measures often obscure underlying geometric details. In this Letter, we introduce a powerful framework, termed multi-bipartition entanglement tomography, which probes the fine structure of entanglement across an exhaustive ensemble of distinct bipartitions. Our cornerstone is the discovery of a “bond-additive law”, which reveals that the entanglement entropy can be precisely decomposed into a bulk volume-law baseline plus a geometric correction formed by a sum of local contributions from crossed bonds of varying ranges. This law distills complex entanglement landscapes into a concise set of entanglement bond tensions $\{\omega_j\}$, serving as a quantitative fingerprint of interaction locality. By applying this tomography to Hamiltonian dynamics, random quantum circuits, and Floquet dynamics, we resolve a fundamental distinction between thermalization mechanisms: Hamiltonian thermalized states retain a persistent geometric imprint characterized by a significantly non-zero ω_1 , while this structure is completely erased in random quantum circuit and Floquet dynamics. Our work establishes multi-bipartition entanglement tomography as a versatile toolbox for the geometric structure of quantum information in many-body systems.

Introduction.—Entanglement entropy (EE) has become a central tool for understanding non-equilibrium quantum dynamics, from characterizing thermalization to revealing information scrambling [1–8]. In both thermal Hamiltonian systems [9–36] and generic random quantum circuits (RQCs) [37–55], the EE typically exhibits rapid growth over time and saturates near the Haar measure average value [56–60]. Within this prevailing paradigm, the late-time evolved state is regarded as a featureless volume-law ensemble, having effectively discarded memory of its microscopic interaction structure and initial-state configurations [14, 61–67].

However, a fundamental conceptual tension remains: unlike random circuits, Hamiltonian dynamics are strictly constrained by conservation laws, most notably energy conservation [36, 68–71]. While it is recognized that this constraint prevents the system from exploring the full Hilbert space like a Haar-random unitary, the precise structural consequences for quantum entanglement remain unexplored. Current paradigms often view the Hamiltonian thermalized state as featureless within an energy shell, leaving an important question unanswered: does the locality of physical interactions leave a persistent, discernible fingerprint on the geometry of entanglement for the Hamiltonian thermalized states?

In this Letter, we resolve this mystery by introducing multi-bipartition entanglement tomography—a framework that systematically probes the fine structure of entanglement across a vast ensemble of geometrically distinct bipartitions. Unlike standard approaches that rely on a single fixed cut, e.g., the conventional half-chain EE, our method provides a comprehensive, high-resolution

characterization of the entanglement landscape. By parameterizing each bipartition according to its boundary geometry, specifically, the number of “crossed bonds” $\{n_j\}$ spanning different ranges (see Fig. 1(a)), we transform a single entropy value into a multi-dimensional map of quantum information.

This comprehensive geometric description leads to our central discovery: the EE of Hamiltonian thermalized states remarkably obeys a simple *bond-additive law*. This principle posits that the EE of an arbitrary bipartition can be precisely decomposed into a bulk volume-law baseline and a sum of local contributions from crossed bonds, distilling the complex entanglement landscape into a concise set of entanglement bond tensions $\{\omega_j\}$. These tensions serve as a quantitative fingerprint, capturing both the Hamiltonian’s underlying locality and the fine structure of the quantum entanglement. As a glimpse, Fig. 1(b) reveals a highly structured distribution in the saturated EEs of thermal Hamiltonian, manifested as a pronounced linear dependence on the number of nearest-neighbor (NN) crossed bonds (n_1), that is entirely absent in RQC and Floquet dynamics. Specifically, we identify a robust hierarchy, $\omega_1 \gg \omega_j$ for $j > 1$, which quantitatively captures the enduring geometric imprint of Hamiltonian locality. Our findings demonstrate that energy conservation compels the system to thermalize coherently along a persistent geometric skeleton defined by the locality of its Hamiltonian. Ultimately, our work establishes a versatile framework for deciphering the geometric origins of entanglement and provides new insights into the paradigm of thermalization in quantum many-body systems.

Model and Methods.—We investigate the dynamics of

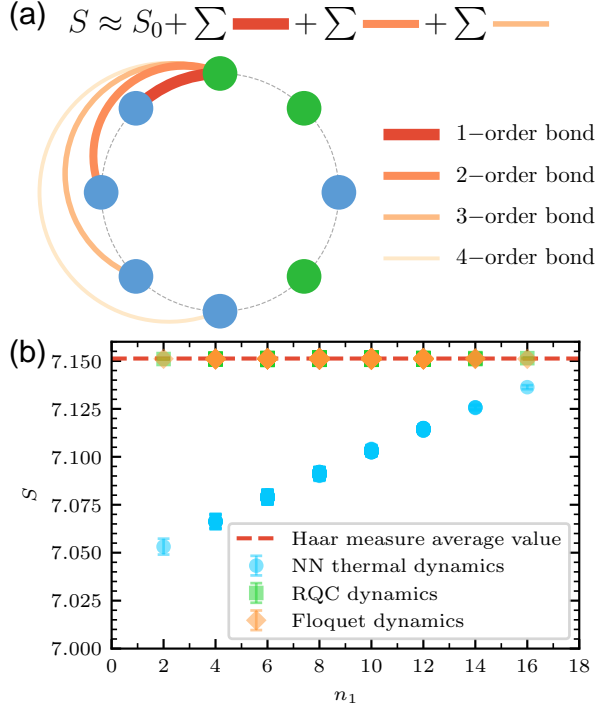


FIG. 1. (a) Schematic illustration of a bipartition for a chain with periodic boundary condition. The spins represented by the green and blue circles constitute subsystem A and its complement, respectively. Examples of crossed bonds with different orders connecting to the top spin are shown. (b) Saturated EEs of equal-sized bipartitions as a function of the crossed 1-order bonds number n_1 for chain length $L = 16$. The NN thermal dynamics governed by $\hat{H}_{\text{NN}}(W = 0.5)$ (evolution time $t = 1000.0$) shows a structured distribution that remains below the Haar measure average value. In contrast, RQC (evolution depth 2000) and Floquet (evolution period number 100) dynamics make saturated EEs perfectly reproduce the Haar measure average. All these results are averaged over 1000 random samples.

a one-dimensional spin-1/2 chain of length L with periodic boundary conditions. Our primary model is the disordered XXZ Hamiltonian with NN spin interactions:

$$\hat{H}_{\text{NN}} = \sum_{i=1}^L \left(\hat{S}_i^x \hat{S}_{i+1}^x + \hat{S}_i^y \hat{S}_{i+1}^y + J_z \hat{S}_i^z \hat{S}_{i+1}^z + h_i \hat{S}_i^z \right), \quad (1)$$

where \hat{S}_i^α are spin-1/2 operators on site i , $J_z = 0.5$, and random fields $h_i \in [-W, W]$ are drawn uniformly. We set $W = 0.5$ to ensure the system resides in the ergodic thermal phase (see Supplemental Material (SM) Sec. II for phase diagnostics). Thus, $\hat{H}_{\text{NN}}(W = 0.5)$ govern a *NN thermal dynamics*. All results are obtained by initializing the system in a product state.

Our primary probe is the von Neumann EE:

$$S = -\text{Tr}(\hat{\rho}_A \log_2 \hat{\rho}_A), \quad (2)$$

where $\hat{\rho}_A$ is the reduced density operator of a subsystem A which contains n_0 spins. By analyzing the EEs

for distinct bipartitions of subsystem A (see SM Sec. III for details), we uncover the fine structure of entanglement and reveal a persistent geometric imprint of the Hamiltonian's locality throughout the entire evolution. To quantitatively describe this fine structure, we characterize each bipartition not only by its size n_0 but also by its detailed geometric properties. Conceptually, any pair of spins in the chain can be connected by a bond. A bond connecting spins separated by a distance j is termed a j -order bond. For a given bipartition, a bond is defined to be “crossed” if its two endpoint spins reside in the subsystem A and its complement, respectively (see Fig. 1(a)). We denote the number of crossed j -order bonds as n_j , e.g., n_1 represents the number of domain walls for the given bipartition. The set $\{n_j\}$ provides a geometric label for each bipartition.

Results.—The unique nature of Hamiltonian thermalization becomes immediately apparent when we examine the entanglement structure through our geometric lens. As a first illustration, Fig. 1(b) plots the saturated EEs for all symmetry-inequivalent bipartitions with equal-sized subsystems ($n_0 = L/2$) as a function of the number of crossed NN bonds, n_1 . The result is striking: for the thermal state evolved under Hamiltonian $\hat{H}_{\text{NN}}(W = 0.5)$, the values of EE form a highly structured distribution with a dominant linear dependence on n_1 . This stands in significant contrast to the dynamics of RQCs and the Floquet system (see SM Sec. I for detailed setup), where all the saturated EEs collapse to almost completely the Haar measure average value, irrespective of the boundary geometry n_1 of the bipartition. This pronounced dependence on local boundary structure provides a compelling first signature of persistent locality within the thermalized state under Hamiltonian dynamics. However, fully resolving the finer geometric architecture of entanglement requires a systematic analysis with the contributions of longer-range bonds.

To fully dissect this geometric entanglement structure, we introduce the framework of *multi-bipartition entanglement tomography*. This framework leverages the EEs under a comprehensive set of bipartitions as a high-resolution probe to characterize the system's entanglement landscape. By parameterizing each bipartition with its geometric labels $\{n_j\}$, we can search for underlying quantitative principles. This tomographic approach determines a set of entanglement bond tensions, $\{\omega_j\}$, that optimally reconstruct the EE for a fixed subsystem size n_0 via the following linear ansatz:

$$S_{\text{fitted}} = S_0 + \sum_{j=1}^{L/2-1} \omega_j n_j. \quad (3)$$

Here, the entanglement bond tensions $\{\omega_j\}$ are determined by a least-squares fit to the numerical data. The sum is truncated at $j = L/2 - 1$ because the set of variables $\{n_1, n_2, \dots, n_{L/2}\}$ is not linearly independent due

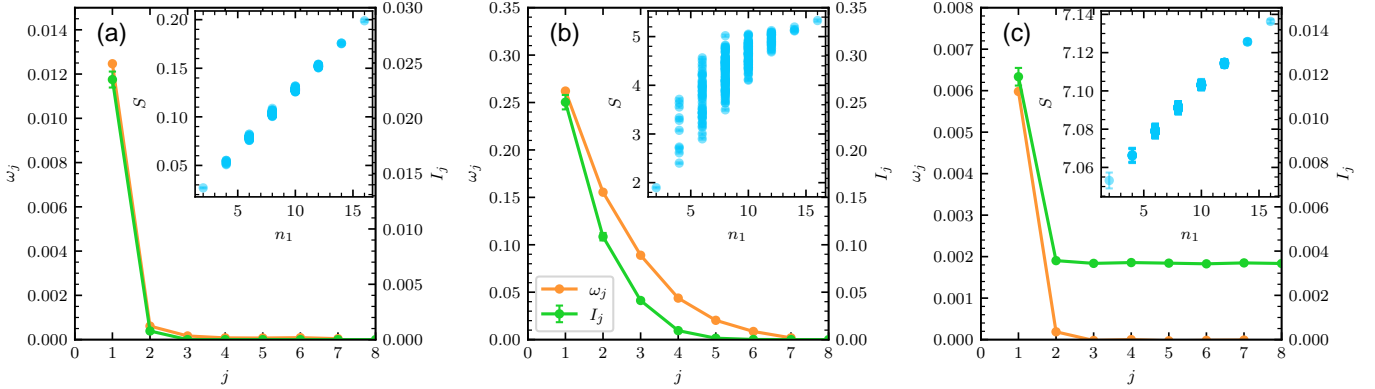


FIG. 2. Evolution of the entanglement structure and mutual information in NN thermal dynamics for $L = 16$. The panels compare the entanglement bond tensions $\{\omega_j\}$ and the mutual informations $\{I_j\}$ at three distinct stages: (a) early time ($t = 0.1$), (b) intermediate time ($t = 2.0$), and (c) late time ($t = 1000.0$) at which the entanglement has saturated. The entanglement bond tensions $\{\omega_j\}$ are extracted from linear regression on the EEs of equal-sized bipartitions ($n_0 = L/2 = 8$), whose raw distributions against n_1 are shown in the corresponding insets. The excellent quality of the fits is confirmed by the high coefficients of determination, $R^2 \approx 0.9993$ (a), $R^2 \approx 0.9959$ (b), and $R^2 \approx 0.9995$ (c). The persistence of the hierarchy $\omega_1 \gg \omega_j$ for $j > 1$ in panel (c) demonstrates a lasting imprint of locality in the thermalized state. All the data of mutual informations and EEs used for fitting are averaged over 1000 random samples.

to $\sum_{j=1}^{L/2} n_j = n_0 (L - n_0)$. As exemplified for the NN thermal dynamics in Fig. 2, this ansatz describes the data with extraordinary precision, yielding coefficients of determination R^2 consistently near unity. This remarkable agreement reveals a fundamental organizing principle, which we term the *bond-additive law*. Physically, this law interprets the EE as an energy-like cost function where the extensive term S_0 provides the volume-law baseline, and the bond-additive terms $\sum \omega_j n_j$ represent the surface tension or geometrical penalty associated with the bipartition boundary. The validity of this law implies that, even within the volume-law entanglement, the system retains a fine-grained structure where cutting a specific j -order bond incurs a quantized entanglement penalty ω_j .

The evolution of these entanglement bond tensions, $\{\omega_j\}$, provides a detailed, dynamical picture of how entanglement geometry is shaped by the local, energy-conserving Hamiltonian. We now apply this analysis to the NN thermal dynamics, with the results shown in Fig. 2. At an early time ($t = 0.1$, Fig. 2(a)), the dynamics are dominated by the Hamiltonian's locality. Entanglement is primarily generated between NN spins, which is perfectly captured by a sharp hierarchy in the entanglement bond tensions: $\omega_1 \gg \omega_j$ for $j > 1$. As the system evolves to an intermediate time ($t = 2.0$, Fig. 2(b)), entanglement propagates through the chain. This is reflected in the significant growth of longer-range entanglement bond tensions such as $\omega_2, \omega_3, \dots$, leading to a more scattered EE distribution as seen in the inset. Most strikingly, at the late time ($t = 1000.0$, Fig. 2(c)) when the EE has saturated, this hierarchy persists. While the absolute values of $\{\omega_j\}$ have decreased as the EE becomes dominated by a large volume-law term S_0 , the shortest-

range contribution ω_1 remains significantly larger than the others. This central result reveals that the state evolved by a thermal Hamiltonian for a long enough time is not structurally random but retains a strong geometric imprint of the Hamiltonian's locality. This persistence is a direct consequence of energy conservation of local Hamiltonians, a fundamental constraint absent in RQCs and Floquet systems, where the entanglement geometry is completely washed out upon saturation, leading to a featureless state where all entanglement bond tensions $\{\omega_j\}$ approach zero.

To understand the microscopic origin of this persistent pattern, we track the evolution of $\{\omega_j\}$ alongside the two-point mutual information $I_j = S_{\{1\}} + S_{\{1+j\}} - S_{\{1,1+j\}}$, where $S_{\{1\}}$, $S_{\{1+j\}}$ and $S_{\{1,1+j\}}$ are respectively the entropies of the first spin, the $(1+j)$ -th spin and their union. I_j quantifies the correlation between two spins separated by a distance j . As shown in Fig. 2, the evolution of $\{I_j\}$ mirrors that of $\{\omega_j\}$. Initially, correlations build up locally, with I_1 dominating. Subsequently, correlations propagate, leading to the growth of longer-range I_j . Most importantly, even after the system has saturated to a thermal state at late time, a distinct hierarchy $I_1 > I_j$ for $j > 1$ persists. This behavior provides a clear, microscopic picture that complements our findings from the multi-bipartition entanglement tomography. The enduring dominance of the NN correlation I_1 is a direct signature of the Hamiltonian's underlying locality. This persistent hierarchy is a consequence of energy conservation, which constrains the system's exploration of Hilbert space and prevents the formation of a featureless Haar-random state. However, it is important to distinguish the roles between $\{I_j\}$ and $\{\omega_j\}$. While I_j detects the presence of local correlations, it is a purely

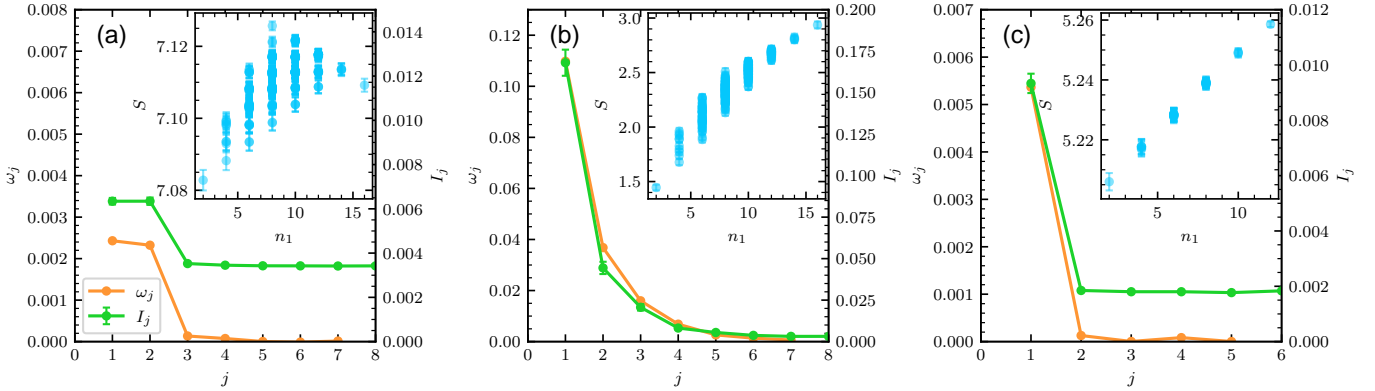


FIG. 3. Entanglement bond tensions $\{\omega_j\}$ with $n_0 = L/2$ and mutual informations $\{I_j\}$ at saturation of other Hamiltonian dynamics. (a) NNN thermal dynamics ($L = 16$, $t = 1000.0$, $R^2 \approx 0.9986$). (b) MBL dynamics ($L = 16$, $t = 10^{12}$, $R^2 \approx 0.9984$). (c) mixed-field dynamics ($L = 12$, $t = 1000.0$, $R^2 \approx 0.9990$). All these results are averaged over 1000 random samples.

local measure. The bond-additive law reveals a far more non-trivial many-body phenomenon as these local correlations do not scramble into a complex, non-linear web, but instead add up coherently to determine the global EE of macroscopic subsystems.

To explore how the bond-additive law holds and how the entanglement geometry manifests for other Hamiltonian dynamical systems, we investigated the following three other scenarios (all of their detailed setups are in SM Sec. I). The values of R^2 that are consistently very close to unity indicate that the bond-additive law also holds in these cases.

Our analysis has established that the persistent $\{\omega_j\}$ hierarchy is a direct fingerprint of the Hamiltonian's interaction range. A natural and powerful test of this hypothesis is to examine a system with a modified locality. To this end, we perform the same tomography on a *next-nearest-neighbor (NNN) thermal dynamics* which is governed by \hat{H}_{NNN} that is extended to include NNN spin interactions. Fig. 3(a) shows the results of the saturated state under \hat{H}_{NNN} , which perfectly align with our hypothesis. The addition of NNN couplings significantly boosts the second entanglement bond tension ω_2 , elevating it to a value comparable to ω_1 . This change in the entanglement geometry is mirrored in the two-point correlations, where the mutual information I_2 also becomes comparable to I_1 . This result provides compelling validation for our multi-bipartition entanglement tomography: the entanglement bond tensions $\{\omega_j\}$ are not just abstract fitting parameters but serve as a quantitative and predictive measure of the Hamiltonian's underlying interaction geometry.

To explore a non-ergodic phase, we apply our method to many-body localized (MBL) [72–86] dynamics, which is governed by $\hat{H}_{\text{NN}}(W = 5.0)$. The saturated state exhibits a profoundly different entanglement structure, as shown in Fig. 3(b). The inset shows an obviously small and highly dispersive EE distribution, a hallmark of non-

ergodicity. The structure of our quantitative probes further reveals the specific details that distinguish MBL from thermalization. The leading entanglement bond tension ω_1 and mutual information I_1 , which capture the shortest-range entanglement and correlation, are more than one order of magnitude larger than those in the thermal case. Besides, the long tail of ω_j reflects the phenomenological l-bit picture of MBL [87–95], where entanglement is generated by effective interactions that decay exponentially with distance but remain non-zero at long ranges.

Finally, we demonstrate the universality of these findings by extending our analysis to dynamics lacking $U(1)$ symmetry. We first consider a disordered mixed-field Hamiltonian, \hat{H}_{MF} , which breaks particle-number conservation while remaining strictly energy-conserving. Evolving initial product states that span multiple charge sectors, we find that the late-time entanglement structure [Fig. 3(c)] exhibits a hierarchy of $\{\omega_j\}$ and $\{I_j\}$ qualitatively identical to the $U(1)$ -symmetric cases. This confirms that the geometric memory of entanglement is a robust consequence of energy conservation, persisting even when the Hilbert space exploration is no longer restricted to a single particle-number sector. A similar robustness is observed for the original \hat{H}_{NN} model when initialized with sector-unrestricted product states (see SM Sec. V). These results establish the geometric imprint of locality as a universal signature of Hamiltonian thermalization, independent of additional symmetry constraints.

Discussion and Conclusion.—In this Letter, we introduce multi-bipartition entanglement tomography, a powerful framework for characterizing the fine geometric structure of entanglement in quantum many-body systems. By applying this framework to Hamiltonian dynamics initialized from product states, we discovered an extraordinarily precise organizing principle: the bond-additive law. This law distills the complex entanglement landscape into a concise set of entanglement bond ten-

sions, $\{\omega_j\}$, which serve as a quantitative fingerprint of the system's entanglement geometry.

Our framework reveals a fundamental distinction in thermalization rooted strictly in energy conservation. While the prevailing paradigm often regards late-time thermalized states as featureless volume, our results demonstrate that Hamiltonian thermalization is intrinsically structured. The persistent hierarchy of entanglement bond tensions ($\omega_1 \gg \omega_j$) demonstrates that energy conservation, as a rigid constraint, prevents the system from erasing its geometric memory. This contrasts with the featureless thermal states produced by RQC and Floquet dynamics. These findings have far-reaching implications for the fundamental theory of quantum thermalization, establishing that the Hamiltonian dynamics retains a fine-grained information structure.

Furthermore, multi-bipartition entanglement tomography provides a powerful lens through which to characterize quantum states. While recent studies have increasingly underscored the importance of multi-bipartition perspectives in understanding many-body systems [96–102], our work establishes the direct and quantitative bridge between the global geometry of entanglement and the local interaction patterns of the Hamiltonian. By demonstrating this correspondence, we provide a universal and quantitative framework to distinguish and classify diverse quantum phases and their non-equilibrium dynamics through the geometric structure of quantum entanglement.

Looking ahead, the versatility of multi-bipartition tomography opens several exciting avenues. Its extension to higher dimensions provides a promising route for isolating universal subleading corrections to the entanglement area law, such as the topological EE in topologically ordered states [103, 104] or the corner coefficients that characterize critical systems and conformal field theories [105, 106]. Additionally, our approach offers a strategy for addressing the inverse problem: reconstructing underlying Hamiltonian properties from the spectrum of entanglement bond tensions $\{\omega_j\}$. Experimentally, our framework is readily accessible, as the requisite EEs can be obtained via randomized measurements [107] or classical shadow tomography [108–113] with no experimental overhead compared to conventional half-chain EE measurements. Our work thus establishes entanglement tomography not just as a conceptual framework, but as a practical and powerful new lens for probing the geometric structure of quantum information in experiments.

Acknowledgement.— C.Y.Z. and Z.X.L. are supported by the National Natural Science Foundation of China under Grant Nos. 12347107 and 12474146, and Beijing Natural Science Foundation under Grant No. JR25007. S.X.Z is supported by Quantum Science and Technology-National Science and Technology Major Project (No. 2024ZD0301700) and the National Natural Science Foundation of China (No. 12574546).

* shixinzhang@iphy.ac.cn

† zixiangli@iphy.ac.cn

- [1] P. Calabrese and J. Cardy, Entanglement entropy and quantum field theory, *J. Stat. Mech.: Theory Exp.* **2004**, P06002 (2004).
- [2] J. Eisert, M. Cramer, and M. B. Plenio, Colloquium: Area laws for the entanglement entropy, *Rev. Mod. Phys.* **82**, 277 (2010).
- [3] A. M. Kaufman, M. E. Tai, A. Lukin, M. Rispoli, R. Schittko, P. M. Preiss, and M. Greiner, Quantum thermalization through entanglement in an isolated many-body system, *Science* **353**, 794 (2016).
- [4] T. Nishioka, Entanglement entropy: Holography and renormalization group, *Rev. Mod. Phys.* **90**, 035007 (2018).
- [5] A. Hamma, S. Santra, and P. Zanardi, Quantum entanglement in random physical states, *Phys. Rev. Lett.* **109**, 040502 (2012).
- [6] T. Zhou and D. J. Luitz, Operator entanglement entropy of the time evolution operator in chaotic systems, *Phys. Rev. B* **95**, 094206 (2017).
- [7] B. Bertini, P. Kos, and T. c. v. Prosen, Entanglement spreading in a minimal model of maximal many-body quantum chaos, *Phys. Rev. X* **9**, 021033 (2019).
- [8] D. Toniolo and S. Bose, Dynamical α -rényi entropies of local hamiltonians grow at most linearly in time, *Phys. Rev. X* **15**, 031046 (2025).
- [9] J. M. Deutsch, Quantum statistical mechanics in a closed system, *Phys. Rev. A* **43**, 2046 (1991).
- [10] M. Srednicki, Chaos and quantum thermalization, *Phys. Rev. E* **50**, 888 (1994).
- [11] M. Srednicki, The approach to thermal equilibrium in quantized chaotic systems, *Journal of Physics A: Mathematical and General* **32**, 1163 (1999).
- [12] M. Rigol, V. Dunjko, and M. Olshanii, Thermalization and its mechanism for generic isolated quantum systems, *Nature* **452**, 854 (2008).
- [13] J. M. Deutsch, Eigenstate thermalization hypothesis, *Reports on Progress in Physics* **81**, 082001 (2018).
- [14] C. Gogolin and J. Eisert, Equilibration, thermalisation, and the emergence of statistical mechanics in closed quantum systems, *Reports on Progress in Physics* **79**, 056001 (2016).
- [15] G. Biroli, C. Kollath, and A. M. Läuchli, Effect of rare fluctuations on the thermalization of isolated quantum systems, *Phys. Rev. Lett.* **105**, 250401 (2010).
- [16] H. Kim and D. A. Huse, Ballistic spreading of entanglement in a diffusive nonintegrable system, *Phys. Rev. Lett.* **111**, 127205 (2013).
- [17] T. Rakovszky, F. Pollmann, and C. W. von Keyserlingk, Sub-ballistic growth of rényi entropies due to diffusion, *Phys. Rev. Lett.* **122**, 250602 (2019).
- [18] P. Łydżba, M. Mierzejewski, M. Rigol, and L. Vidmar, Generalized thermalization in quantum-chaotic quadratic hamiltonians, *Phys. Rev. Lett.* **131**, 060401 (2023).
- [19] D. K. Mark, F. Surace, A. Elben, A. L. Shaw, J. Choi, G. Refael, M. Endres, and S. Choi, Maximum entropy principle in deep thermalization and in hilbert-space ergodicity, *Phys. Rev. X* **14**, 041051 (2024).
- [20] A. Riera-Campeny, A. Sanpera, and P. Strasberg, *Phys. Rev. X* **14**, 041052 (2024).

berg, Quantum systems correlated with a finite bath: Nonequilibrium dynamics and thermodynamics, *PRX Quantum* **2**, 010340 (2021).

[21] D. Jansen, J. Stolpp, L. Vidmar, and F. Heidrich-Meisner, Eigenstate thermalization and quantum chaos in the holstein polaron model, *Phys. Rev. B* **99**, 155130 (2019).

[22] J. C. Louw and S. Kehrein, Thermalization of many many-body interacting sachdev-ye-kitaev models, *Phys. Rev. B* **105**, 075117 (2022).

[23] M. Rigol, Quantum quenches and thermalization in one-dimensional fermionic systems, *Phys. Rev. A* **80**, 053607 (2009).

[24] M. Rigol and L. F. Santos, Quantum chaos and thermalization in gapped systems, *Phys. Rev. A* **82**, 011604 (2010).

[25] N. Linden, S. Popescu, A. J. Short, and A. Winter, Quantum mechanical evolution towards thermal equilibrium, *Phys. Rev. E* **79**, 061103 (2009).

[26] L. F. Santos and M. Rigol, Onset of quantum chaos in one-dimensional bosonic and fermionic systems and its relation to thermalization, *Phys. Rev. E* **81**, 036206 (2010).

[27] C. Neuenhahn and F. Marquardt, Thermalization of interacting fermions and delocalization in fock space, *Phys. Rev. E* **85**, 060101 (2012).

[28] S. Khlebnikov and M. Kruczenski, Locality, entanglement, and thermalization of isolated quantum systems, *Phys. Rev. E* **90**, 050101 (2014).

[29] D. Hahn, J.-D. Urbina, K. Richter, R. Dubertrand, and S. L. Sondhi, Ergodic and nonergodic many-body dynamics in strongly nonlinear lattices, *Phys. Rev. E* **103**, 052213 (2021).

[30] M. H. Muñoz Arias, Statistical complexity and the road to equilibrium in many-body chaotic quantum systems, *Phys. Rev. E* **106**, 044103 (2022).

[31] V. P. Pavlov, Y. R. Chorbadzhiyska, C. Nation, D. Porras, and P. A. Ivanov, Random matrix theory approach to quantum fisher information in quantum ergodic systems, *Phys. Rev. E* **110**, 024135 (2024).

[32] Y. R. Chorbadzhiyska and P. A. Ivanov, Onset of quantum thermalization in the jahn-teller model, *Phys. Rev. E* **110**, 044127 (2024).

[33] L. D'Alessio, Y. Kafri, A. Polkovnikov, and M. Rigol, From quantum chaos and eigenstate thermalization to statistical mechanics and thermodynamics, *Advances in Physics* **65**, 239 (2016).

[34] M. Mezei and D. Stanford, On entanglement spreading in chaotic systems, *J. High Energy Phys.* **2017**, 65 (2017).

[35] E. Bianchi, L. Hackl, and N. Yokomizo, Linear growth of the entanglement entropy and the Kolmogorov-Sinai rate, *J. High Energy Phys.* **2018**, 25 (2018).

[36] C. M. Langlett and J. F. Rodriguez-Nieva, Entanglement patterns of quantum chaotic hamiltonians with a scalar u(1) charge, *Phys. Rev. Lett.* **134**, 230402 (2025).

[37] R. Oliveira, O. C. O. Dahlsten, and M. B. Plenio, Generic entanglement can be generated efficiently, *Phys. Rev. Lett.* **98**, 130502 (2007).

[38] A. Nahum, J. Ruhman, S. Vijay, and J. Haah, Quantum entanglement growth under random unitary dynamics, *Phys. Rev. X* **7**, 031016 (2017).

[39] C. W. von Keyserlingk, T. Rakovszky, F. Pollmann, and S. L. Sondhi, Operator hydrodynamics, otocs, and entanglement growth in systems without conservation laws, *Phys. Rev. X* **8**, 021013 (2018).

[40] A. Nahum, S. Vijay, and J. Haah, Operator spreading in random unitary circuits, *Phys. Rev. X* **8**, 021014 (2018).

[41] T. Zhou and A. Nahum, Emergent statistical mechanics of entanglement in random unitary circuits, *Phys. Rev. B* **99**, 174205 (2019).

[42] Y. Li, X. Chen, and M. P. A. Fisher, Measurement-driven entanglement transition in hybrid quantum circuits, *Phys. Rev. B* **100**, 134306 (2019).

[43] B. Skinner, J. Ruhman, and A. Nahum, Measurement-induced phase transitions in the dynamics of entanglement, *Phys. Rev. X* **9**, 031009 (2019).

[44] C.-M. Jian, Y.-Z. You, R. Vasseur, and A. W. W. Ludwig, Measurement-induced criticality in random quantum circuits, *Phys. Rev. B* **101**, 104302 (2020).

[45] A. Lerose, M. Sonner, and D. A. Abanin, Influence matrix approach to many-body floquet dynamics, *Phys. Rev. X* **11**, 021040 (2021).

[46] S. Liu, M.-R. Li, S.-X. Zhang, S.-K. Jian, and H. Yao, Universal kardar-parisi-zhang scaling in noisy hybrid quantum circuits, *Phys. Rev. B* **107**, L201113 (2023).

[47] M. P. Fisher, V. Khemani, A. Nahum, and S. Vijay, Random quantum circuits, *Annu. Rev. Condens. Matter Phys.* **14**, 335 (2023).

[48] Y. Han and X. Chen, Entanglement dynamics in U(1) symmetric hybrid quantum automaton circuits, *Quantum* **7**, 1200 (2023).

[49] S. Liu, M.-R. Li, S.-X. Zhang, S.-K. Jian, and H. Yao, Noise-induced phase transitions in hybrid quantum circuits, *Phys. Rev. B* **110**, 064323 (2024).

[50] S. Liu, M.-R. Li, S.-X. Zhang, and S.-K. Jian, Entanglement structure and information protection in noisy hybrid quantum circuits, *Phys. Rev. Lett.* **132**, 240402 (2024).

[51] S. Liu, H.-K. Zhang, S. Yin, and S.-X. Zhang, Symmetry restoration and quantum mpemba effect in symmetric random circuits, *Phys. Rev. Lett.* **133**, 140405 (2024).

[52] W. Wang, S. Liu, J. Li, S.-X. Zhang, and S. Yin, Driven critical dynamics in measurement-induced phase transitions, *arXiv:2411.06648* (2024).

[53] S. Liu, S.-K. Jian, and S.-X. Zhang, Noisy monitored quantum circuits, *arXiv:2512.18783* (2025).

[54] Y.-Q. Chen, S. Liu, and S.-X. Zhang, Subsystem Information Capacity in Random Circuits and Hamiltonian Dynamics, *Quantum* **9**, 1783 (2025).

[55] K. Chalas, P. Calabrese, and C. Rylands, Quench dynamics of entanglement from crosscap states, *SciPost Phys.* **19**, 132 (2025).

[56] D. N. Page, Average entropy of a subsystem, *Phys. Rev. Lett.* **71**, 1291 (1993).

[57] P. Vivo, M. P. Pato, and G. Oshanin, Random pure states: Quantifying bipartite entanglement beyond the linear statistics, *Phys. Rev. E* **93**, 052106 (2016).

[58] E. Bianchi and P. Donà, Typical entanglement entropy in the presence of a center: Page curve and its variance, *Phys. Rev. D* **100**, 105010 (2019).

[59] R. Patil, L. Hackl, G. R. Fagan, and M. Rigol, Average pure-state entanglement entropy in spin systems with su(2) symmetry, *Phys. Rev. B* **108**, 245101 (2023).

[60] Y. Lu, P. Shi, X.-H. Wang, J. Hu, and S.-J. Ran, Persistent ballistic entanglement spreading with optimal control in quantum spin chains, *Phys. Rev. Lett.*

133, 070402 (2024).

[61] S. Goldstein, J. L. Lebowitz, R. Tumulka, and N. Zanghì, Long-time behavior of macroscopic quantum systems, *The European Physical Journal H* **35**, 173 (2010).

[62] A. Riera, C. Gogolin, and J. Eisert, Thermalization in nature and on a quantum computer, *Phys. Rev. Lett.* **108**, 080402 (2012).

[63] W. W. Ho and S. Choi, Exact emergent quantum state designs from quantum chaotic dynamics, *Phys. Rev. Lett.* **128**, 060601 (2022).

[64] S. Pilatowsky-Cameo, C. B. Dag, W. W. Ho, and S. Choi, Complete hilbert-space ergodicity in quantum dynamics of generalized fibonacci drives, *Phys. Rev. Lett.* **131**, 250401 (2023).

[65] S. Pilatowsky-Cameo, I. Marvian, S. Choi, and W. W. Ho, Hilbert-space ergodicity in driven quantum systems: Obstructions and designs, *Phys. Rev. X* **14**, 041059 (2024).

[66] M. Fava, J. Kurchan, and S. Pappalardi, Designs via free probability, *Phys. Rev. X* **15**, 011031 (2025).

[67] S. Ghosh, C. M. Langlett, N. Hunter-Jones, and J. F. Rodriguez-Nieva, Late-time ensembles of quantum states in quantum chaotic systems, *Phys. Rev. B* **112**, 094302 (2025).

[68] K. Kaneko, E. Iyoda, and T. Sagawa, Characterizing complexity of many-body quantum dynamics by higher-order eigenstate thermalization, *Phys. Rev. A* **101**, 042126 (2020).

[69] J. F. Rodriguez-Nieva, C. Jonay, and V. Khemani, Quantifying quantum chaos through microcanonical distributions of entanglement, *Phys. Rev. X* **14**, 031014 (2024).

[70] L. Mao, L. Cui, T. Schuster, and H.-Y. Huang, Random unitaries that conserve energy, [arXiv:2510.08448](https://arxiv.org/abs/2510.08448) (2025).

[71] L. Cui, T. Schuster, L. Mao, H.-Y. Huang, and F. Brandao, Random unitaries from hamiltonian dynamics, [arXiv:2510.08434](https://arxiv.org/abs/2510.08434) (2025).

[72] M. Žnidarič, T. c. v. Prosen, and P. Prelovšek, Many-body localization in the heisenberg xxz magnet in a random field, *Phys. Rev. B* **77**, 064426 (2008).

[73] A. Pal and D. A. Huse, Many-body localization phase transition, *Phys. Rev. B* **82**, 174411 (2010).

[74] J. H. Bardarson, F. Pollmann, and J. E. Moore, Unbounded growth of entanglement in models of many-body localization, *Phys. Rev. Lett.* **109**, 017202 (2012).

[75] R. Vosk and E. Altman, Many-body localization in one dimension as a dynamical renormalization group fixed point, *Phys. Rev. Lett.* **110**, 067204 (2013).

[76] E. Altman and R. Vosk, Universal dynamics and renormalization in many-body-localized systems, *Annu. Rev. Condens. Matter Phys.* **6**, 383 (2015).

[77] M. Schreiber, S. S. Hodgman, P. Bordia, H. P. Lüschen, M. H. Fischer, R. Vosk, E. Altman, U. Schneider, and I. Bloch, Observation of many-body localization of interacting fermions in a quasirandom optical lattice, *Science* **349**, 842 (2015).

[78] S.-X. Zhang and H. Yao, Universal properties of many-body localization transitions in quasiperiodic systems, *Phys. Rev. Lett.* **121**, 206601 (2018).

[79] A. Lukin, M. Rispoli, R. Schittko, M. E. Tai, A. M. Kaufman, S. Choi, V. Khemani, J. Léonard, and M. Greiner, Probing entanglement in a many-body-localized system, *Science* **364**, 256 (2019).

[80] R. Fan, P. Zhang, H. Shen, and H. Zhai, Out-of-time-order correlation for many-body localization, *Science Bulletin* **62**, 707 (2017).

[81] Y. Huang, Y.-L. Zhang, and X. Chen, Out-of-time-ordered correlators in many-body localized systems, *Annalen der Physik* **529**, 1600318 (2017).

[82] S. Liu, H.-K. Zhang, S. Yin, S.-X. Zhang, and H. Yao, Symmetry restoration and quantum mpemba effect in many-body localization systems, *Science Bulletin* **70**, 3991 (2025).

[83] R.-Q. He and Z.-Y. Lu, Characterizing many-body localization by out-of-time-ordered correlation, *Phys. Rev. B* **95**, 054201 (2017).

[84] K. Slagle, Z. Bi, Y.-Z. You, and C. Xu, Out-of-time-order correlation in marginal many-body localized systems, *Phys. Rev. B* **95**, 165136 (2017).

[85] R. Vosk, D. A. Huse, and E. Altman, Theory of the many-body localization transition in one-dimensional systems, *Phys. Rev. X* **5**, 031032 (2015).

[86] P. Sierant, M. Lewenstein, A. Scardicchio, L. Vidmar, and J. Zakrzewski, Many-body localization in the age of classical computing, *Reports on Progress in Physics* **88**, 026502 (2025).

[87] M. Serbyn, Z. Papić, and D. A. Abanin, Local conservation laws and the structure of the many-body localized states, *Phys. Rev. Lett.* **111**, 127201 (2013).

[88] D. A. Huse, R. Nandkishore, and V. Oganesyan, Phenomenology of fully many-body-localized systems, *Phys. Rev. B* **90**, 174202 (2014).

[89] A. Chandran, I. H. Kim, G. Vidal, and D. A. Abanin, Constructing local integrals of motion in the many-body localized phase, *Phys. Rev. B* **91**, 085425 (2015).

[90] R. Nandkishore and D. A. Huse, Many-body localization and thermalization in quantum statistical mechanics, *Annu. Rev. Condens. Matter Phys.* **6**, 15 (2015).

[91] V. Ros, M. Müller, and A. Scardicchio, Integrals of motion in the many-body localized phase, *Nuclear Physics B* **891**, 420 (2015).

[92] L. Rademaker and M. Ortúño, Explicit local integrals of motion for the many-body localized state, *Phys. Rev. Lett.* **116**, 010404 (2016).

[93] J. Z. Imbrie, V. Ros, and A. Scardicchio, Local integrals of motion in many-body localized systems, *Annalen der Physik* **529**, 1600278 (2017).

[94] D. A. Abanin, E. Altman, I. Bloch, and M. Serbyn, Colloquium: Many-body localization, thermalization, and entanglement, *Rev. Mod. Phys.* **91**, 021001 (2019).

[95] D. Aceituno Chávez, C. Artiaco, T. Klein Kvorning, L. Herviou, and J. H. Bardarson, Ultraslow growth of number entropy in an ℓ -bit model of many-body localization, *Phys. Rev. Lett.* **133**, 126502 (2024).

[96] S. Singha Roy, S. N. Santalla, J. Rodríguez-Laguna, and G. Sierra, Entanglement as geometry and flow, *Phys. Rev. B* **101**, 195134 (2020).

[97] W.-T. Kuo, A. A. Akhtar, D. P. Arovas, and Y.-Z. You, Markovian entanglement dynamics under locally scrambled quantum evolution, *Phys. Rev. B* **101**, 224202 (2020).

[98] A. A. Akhtar and Y.-Z. You, Multiregion entanglement in locally scrambled quantum dynamics, *Phys. Rev. B* **102**, 134203 (2020).

[99] R. Fan, S. Vijay, A. Vishwanath, and Y.-Z. You, Self-organized error correction in random unitary circuits

with measurement, *Phys. Rev. B* **103**, 174309 (2021).

[100] D. Kolisnyk, R. A. Medina, R. Vasseur, and M. Serbyn, Tensor cross interpolation of purities in quantum many-body systems, [arXiv:2503.17230](https://arxiv.org/abs/2503.17230) (2025).

[101] C.-Y. Zhang, Z.-X. Li, and S.-X. Zhang, Entanglement growth from entangled states: A unified perspective on entanglement generation and transport, [arXiv:2510.08344](https://arxiv.org/abs/2510.08344) (2025).

[102] M. Drieb-Schoen, F. Dreier, and W. Lechner, Bundling of bipartite entanglement, [arXiv:2512.16979](https://arxiv.org/abs/2512.16979) (2025).

[103] A. Kitaev and J. Preskill, Topological entanglement entropy, *Phys. Rev. Lett.* **96**, 110404 (2006).

[104] M. Levin and X.-G. Wen, Detecting topological order in a ground state wave function, *Phys. Rev. Lett.* **96**, 110405 (2006).

[105] P. Calabrese and J. Cardy, Entanglement entropy and quantum field theory, *Journal of Statistical Mechanics: Theory and Experiment* **2004**, P06002 (2004).

[106] E. Fradkin and J. E. Moore, Entanglement entropy of 2d conformal quantum critical points: Hearing the shape of a quantum drum, *Phys. Rev. Lett.* **97**, 050404 (2006).

[107] T. Brydges, A. Elben, P. Jurcevic, B. Vermersch, C. Maier, B. P. Lanyon, P. Zoller, R. Blatt, and C. F. Roos, Probing rényi entanglement entropy via randomized measurements, *Science* **364**, 260 (2019).

[108] H.-Y. Huang, R. Kueng, and J. Preskill, Predicting many properties of a quantum system from very few measurements, *Nature Physics* **16**, 1050 (2020).

[109] M. McGinley, S. Leontica, S. J. Garratt, J. Jovanovic, and S. H. Simon, Quantifying information scrambling via classical shadow tomography on programmable quantum simulators, *Phys. Rev. A* **106**, 012441 (2022).

[110] I. Avdic and D. A. Mazziotti, Fewer measurements from shadow tomography with n -representability conditions, *Phys. Rev. Lett.* **132**, 220802 (2024).

[111] S. N. Hearth, M. O. Flynn, A. Chandran, and C. R. Laumann, Efficient local classical shadow tomography with number conservation, *Phys. Rev. Lett.* **133**, 060802 (2024).

[112] Y. Wang, Quantum advantage via efficient postprocessing on qudit classical shadow tomography, *Phys. Rev. Lett.* **135**, 200601 (2025).

[113] S. Zhang, X. Feng, M. Ippoliti, and Y.-Z. You, Holomorphic classical shadow tomography, *Phys. Rev. B* **111**, 054306 (2025).

[114] P. Ponte, Z. Papić, F. m. c. Huveneers, and D. A. Abanin, Many-body localization in periodically driven systems, *Phys. Rev. Lett.* **114**, 140401 (2015).

[115] O. Bohigas, M. J. Giannoni, and C. Schmit, Characterization of chaotic quantum spectra and universality of level fluctuation laws, *Phys. Rev. Lett.* **52**, 1 (1984).

[116] V. Oganesyan and D. A. Huse, Localization of interacting fermions at high temperature, *Phys. Rev. B* **75**, 155111 (2007).

[117] P. Roushan, C. Neill, J. Tangpanitanon, V. M. Bastidas, A. Megrant, R. Barends, Y. Chen, Z. Chen, B. Chiaro, A. Dunsworth, A. Fowler, B. Foxen, M. Giustina, E. Jeffrey, J. Kelly, E. Lucero, J. Mutus, M. Neeley, C. Quintana, D. Sank, A. Vainsencher, J. Wenner, T. White, H. Neven, D. G. Angelakis, and J. Martinis, Spectroscopic signatures of localization with interacting photons in superconducting qubits, *Science* **358**, 1175 (2017).

[118] M. L. Mehta, *Random matrices* (Elsevier, 2004).

[119] Y. Y. Atas, E. Bogomolny, O. Giraud, and G. Roux, Distribution of the ratio of consecutive level spacings in random matrix ensembles, *Phys. Rev. Lett.* **110**, 084101 (2013).

[120] L. D’Alessio and M. Rigol, Long-time behavior of isolated periodically driven interacting lattice systems, *Phys. Rev. X* **4**, 041048 (2014).

Supplemental Material for “Bond Additivity and Persistent Geometric Imprints of Entanglement in Quantum Thermalization”

CONTENTS

I. Description of Dynamical Protocols	9
II. The Level Spacing Ratios Distribution Analysis	12
III. Symmetry Analysis and Enumeration of Bipartition Geometries	12
IV. More Results about Mutual Information	14
V. Detailed Analysis of Fitting Quality and More Fitting Results	14

I. DESCRIPTION OF DYNAMICAL PROTOCOLS

We examine distinct dynamical protocols on a one-dimensional spin-1/2 chain of length L with periodic boundary condition (PBC). For protocols that conserve $U(1)$ particle number, the initial state $|\psi_0\rangle$ is a computational basis state sampled uniformly from the zero-magnetization (half-filling) sector, $\sum_{i=1}^L \hat{S}_i^z = 0$. We consider five particle-number-conserving protocols defined as follows:

Nearest-Neighbor (NN) Thermal Dynamics: This is the primary dynamics we studied, which is governed by a time-independent thermal Hamiltonian:

$$\hat{H}_{\text{NN}} = \sum_{i=1}^L \left(\hat{S}_i^x \hat{S}_{i+1}^x + \hat{S}_i^y \hat{S}_{i+1}^y + J_z \hat{S}_i^z \hat{S}_{i+1}^z + h_i \hat{S}_i^z \right), \quad (\text{S1})$$

where we set the anisotropy to $J_z = 0.5$. The on-site random fields h_i are drawn independently and uniformly from the interval $[-W, W]$ and $W = 0.5$, thus this Hamiltonian is denoted by $\hat{H}_{\text{NN}}(W = 0.5)$.

Next-Nearest-Neighbor (NNN) Thermal Dynamics: This dynamics is designed to explore the effect of longer-range interactions. The NNN couplings are introduced:

$$\hat{H}_{\text{NNN}} = \hat{H}_{\text{NN}}(W = 0.5) + \gamma \sum_{i=1}^L \left(\hat{S}_i^x \hat{S}_{i+2}^x + \hat{S}_i^y \hat{S}_{i+2}^y + J_z \hat{S}_i^z \hat{S}_{i+2}^z \right), \quad (\text{S2})$$

where the NNN interaction strength is set to $\gamma = 24/25$. This Hamiltonian remains in a thermal phase.

Many-Body Localized (MBL) Dynamics: It is realized using the same Hamiltonian as in Eq. (S1), but with a strong disorder strength $W = 5.0$ to drive the system into the MBL phase. Its Hamiltonian is denoted by $\hat{H}_{\text{NN}}(W = 5.0)$.

Random Quantum Circuit (RQC) Dynamics: The circuit is generated by sequentially applying two-qubit unitary gates. In each step, a single gate $\hat{U}_{i,i+1}$ is applied to a randomly chosen adjacent pair of spins $(i, i+1)$ from all L pairs with uniform probability. The unitary is given by:

$$e^{-i\pi(\hat{S}_i^x \hat{S}_{i+1}^x + \hat{S}_i^y \hat{S}_{i+1}^y)/2} e^{-i\pi \hat{S}_i^z \hat{S}_{i+1}^z}, \quad (\text{S3})$$

Floquet Dynamics: The Floquet dynamics is defined by a periodic drive with the Floquet operator:

$$\hat{F} = e^{-iT_0 \hat{H}_0} e^{-iT_1 \hat{H}_1}, \quad (\text{S4})$$

where the two parts of the drive are given by

$$\hat{H}_0 = \sum_{i=1}^L \left(\hat{S}_i^z \hat{S}_{i+1}^z + h_i \hat{S}_i^z \right) \quad (\text{S5})$$

and

$$\hat{H}_1 = \sum_{i=1}^L \left(\hat{S}_i^x \hat{S}_{i+1}^x + \hat{S}_i^y \hat{S}_{i+1}^y \right). \quad (\text{S6})$$

The parameters are set to $T_0 = 1.0$, $T_1 = 2.5$, and the disorder strength in \hat{H}_0 is $W = 5.0$. This setup is adapted from Ref. [114] but implemented with PBC. This protocol is also thermalizing but does not conserve energy due to time-dependence.

Beyond particle number conserved dynamics, we examine two protocols where $U(1)$ symmetry is absent. In these cases, the initial state is a random product state unrestricted by particle-number conservation, allowing the dynamics to explore the full many-body Hilbert space:

$$|\psi_0\rangle = \prod_{i=1}^L \otimes \left(\cos \frac{\theta_i}{2} |\uparrow\rangle + e^{i\phi_i} \sin \frac{\theta_i}{2} |\downarrow\rangle \right), \quad (\text{S7})$$

where random parameters $\{\theta_i\}$ and $\{\phi_i\}$ cause each spin to independently distribute uniformly on the surface of the Bloch sphere.

We first consider evolution under the thermal Hamiltonian \hat{H}_{NN} with $W = 0.5$ [Eq. (S1)]. Unlike configurations restricted to the half-filling sector, these random product states are superpositions spanning multiple magnetization sectors, thereby allowing the dynamics to explore a significantly larger manifold of the many-body Hilbert space.

For the second protocol starting from random product states without $U(1)$ symmetry, we introduce a mixed-field Hamiltonian. This model breaks the conservation of total magnetization by adding a disordered transverse field term to the NN thermal Hamiltonian:

$$\hat{H}_{\text{MF}} = \hat{H}_{\text{NN}}(W = 0.5) + \sum_{i=1}^L g_i \hat{S}_i^x, \quad (\text{S8})$$

where $\{g_j\}$ follows the same distribution as $\{h_j\}$ in $\hat{H}_{\text{NN}}(W = 0.5)$ and is independent of $\{h_j\}$. The corresponding dynamics is called *mixed-field dynamics*.

To provide a clear visual representation of the different dynamical protocols, we present their schematic diagrams in Fig. S1. These diagrams illustrate the distinct structures of (a) time-independent Hamiltonian evolution, (b) the sequential gate application in RQCs, and (c) the periodic driving of the Floquet protocol.

To complement these schematics, Fig. S2 displays the evolution of the half-chain entanglement entropy (HCEE) for each protocol, illustrating the trajectories toward their respective steady states. As shown, the HCEE for the NN thermal, NNN thermal, and mixed-field dynamics effectively saturates by $t = 10^3$. In the MBL dynamics, the system reaches its characteristic steady state by $t = 10^{12}$. Similarly, the RQC and Floquet dynamics achieve full saturation at a circuit depth of 2000 and 100 driving periods, respectively. The analysis throughout the main text utilizes these saturated data points to characterize the late-time entanglement landscape.

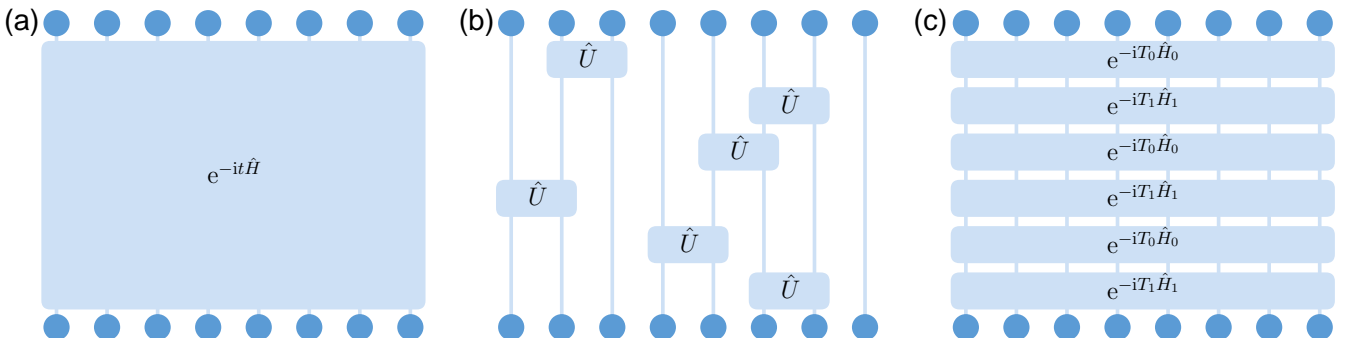


FIG. S1. Schematic illustrations of Hamiltonian dynamics (where $\hat{H}_{\text{NN}}(W = 0.5)$, $\hat{H}_{\text{NN}}(W = 5.0)$, \hat{H}_{NNN} and \hat{H}_{MF} are all represented by \hat{H}) (a), RQC dynamics (b), and Floquet dynamics (c). Blue circles represent spins.

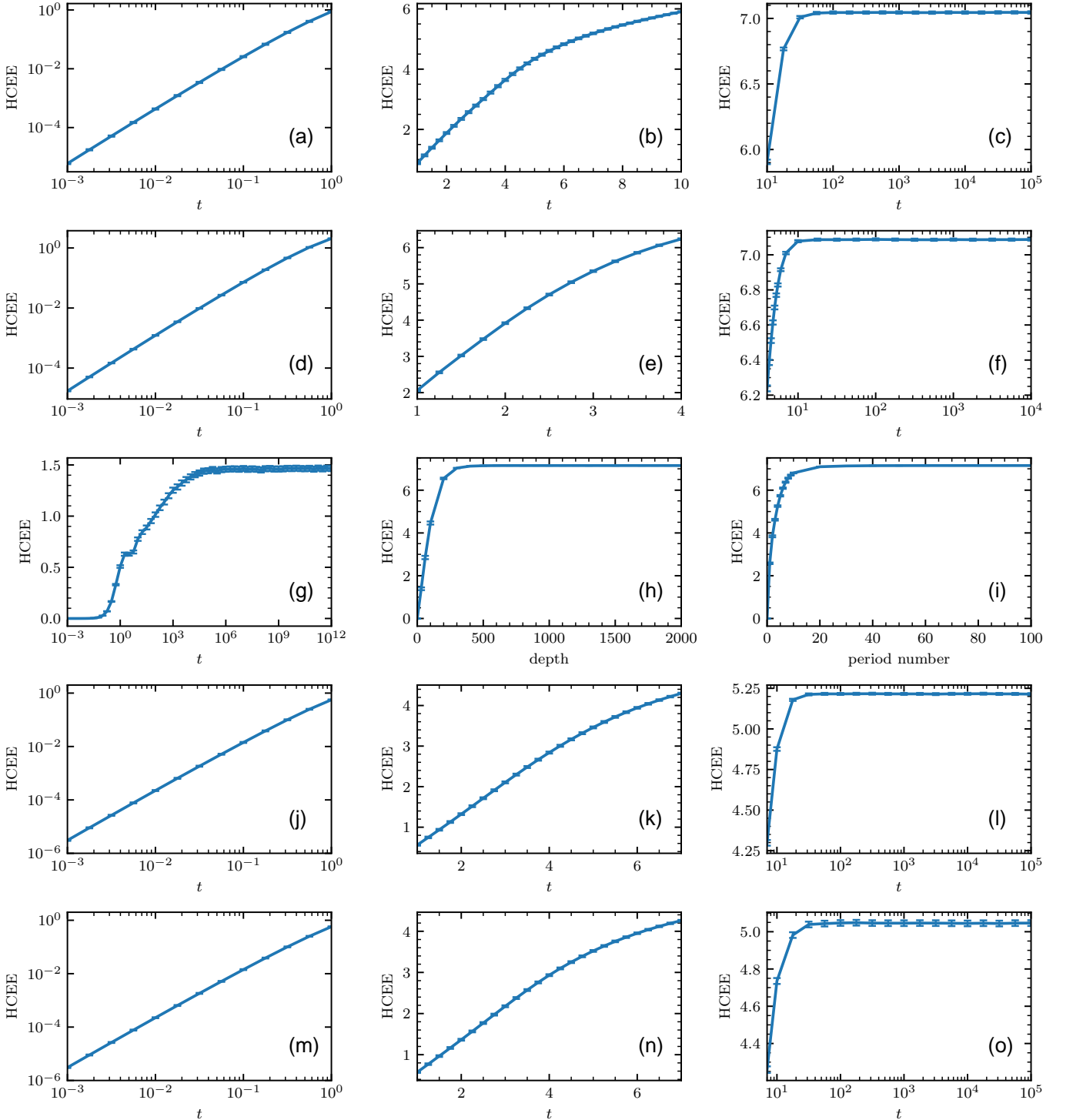


FIG. S2. Evolution of the HCEE for the various dynamics studied. The top row (a-c) displays the HCEE evolution for the NN thermal dynamics, showing the (a) initial linear growth, (b) subsequent slowing, and (c) final saturation. Similarly, the second row (d-f), the fourth row (j-l) and the fifth row (m-o) respectively show the evolution for the NNN thermal dynamics, the mixed-field dynamics and the dynamics governed by $\hat{H}_{\text{NN}}(W = 0.5)$ starting from random product states across the same three regimes. The third row presents the complete HCEE evolution for (g) MBL dynamics, (h) RQC dynamics and (i) Floquet dynamics. For the Hamiltonian dynamics (a-g) and (j-o), the horizontal axis is evolution time t ; for the RQC (h) and Floquet (i) dynamics, it represents the circuit depth and the number of evolution periods, respectively. The simulations for mixed-field dynamics and the dynamics governed by $\hat{H}_{\text{NN}}(W = 0.5)$ starting from random product state are performed on a chain of length $L = 12$, while all other dynamics are performed for $L = 16$. The results for MBL dynamics are averaged over 1000 disorder and initial state realizations, while all other dynamics are averaged over 200 realizations.

II. THE LEVEL SPACING RATIOS DISTRIBUTION ANALYSIS

In this section, we provide proofs for the thermal nature of various dynamics. The distribution of adjacent level spacing ratios, $p(r)$, is a powerful probe for distinguishing between thermal and non-thermal phases, a method rooted in random matrix theory [73, 115–118]. We apply this diagnostic to the four Hamiltonians ($\hat{H}_{\text{NN}}(W = 0.5)$, \hat{H}_{NNN} , $\hat{H}_{\text{NN}}(W = 5.0)$ and \hat{H}_{MF}) and the Floquet operator \hat{F} to confirm their dynamical character.

We perform exact diagonalization for \hat{H}_{MF} and other operators in the whole Hilbert space and within the half-filling sector where $\hat{S}_{\text{tot}}^z = \sum_{i=1}^L \hat{S}_i^z = 0$, respectively. For the Hamiltonian systems, we analyze the middle one-third of the sorted eigenenergy spectrum, a standard procedure consistent with Ref. [73]. For Floquet operator $\hat{F} = e^{-iT_0\hat{H}_0}e^{-iT_1\hat{H}_1}$, we analyze all of its eigenvalues $\{e^{-i\theta_k}\}$ and set the quasienergies $\{\theta_k\}$ within range $[-\pi, \pi]$.

Given a list of eigenenergies $\{E_k\}$ or quasienergies $\{\theta_k\}$ sorted in ascending order, the consecutive level spacings are defined as $\delta_k = E_{k+1} - E_k$ or $\delta_k = \theta_{k+1} - \theta_k$, respectively. The level spacing ratio r_k is then defined as the ratio of the smaller to the larger of two consecutive spacings:

$$r_k = \frac{\min(\delta_k, \delta_{k+1})}{\max(\delta_k, \delta_{k+1})}. \quad (\text{S9})$$

From the collection of all such ratios, we construct the histograms of $\{r_k\}$ of all cases, presented in Fig. S3, along with the numerical average values \bar{r} .

This diagnostic tool provides a sharp distinction between different dynamical regimes. For the thermal cases of our models, the histograms of $\{r_k\}$ for Hamiltonian systems and Floquet system are expected to follow the Gaussian Orthogonal Ensemble (GOE) and the Circular Orthogonal Ensemble (COE), respectively. In contrast, the MBL phase is characterized by a Poisson distribution. As shown in Fig. S3, our numerical results align perfectly with corresponding theoretical baselines. The distributions for the three thermal Hamiltonians and the Floquet operator match the GOE and COE curves, confirming they are in the thermal regime. Conversely, the MBL Hamiltonian follows the Poisson distribution, a clear signature of its MBL nature. All these are further corroborated by \bar{r} for each case, which closely matches the theoretical average value of the corresponding distribution: $\langle r \rangle_{\text{GOE}} = 4 - 2\sqrt{3} \approx 0.536$ [119], $\langle r \rangle_{\text{COE}} \approx 0.527$ [120] and $\langle r \rangle_{\text{Poisson}} = 2 \ln 2 - 1 \approx 0.386$ [119].

III. SYMMETRY ANALYSIS AND ENUMERATION OF BIPARTITION GEOMETRIES

A central aspect of our methodology is the simplification of the analysis by exploiting the system's symmetries. As mentioned in the main text, our analysis involves averaging over various sources of randomness (e.g., initial states, disorders, and circuit realizations). This procedure, combined with the PBC, restores both translational and parity symmetries to the ensemble-averaged system.

These symmetries have two crucial consequences that greatly reduce the complexity of our analysis:

1. The mutual information between any two spins depends solely on their separation distance j , and we denote it as I_j .
2. The analysis of EE across all $2^{L-1} - 1$ nontrivial bipartitions can be reduced to studying a much smaller, minimal set of symmetry-inequivalent representative bipartitions.

For a one-dimensional spin chain of even length L , there are 2^L ways to form a subsystem A. However, since the EE is symmetric with respect to the subsystem and its complement, we only consider bipartitions where the subsystem size n_0 does not exceed half the chain length, i.e., $n_0 \leq L/2$. The case $n_0 = 0$ is trivial. Thus, the total number of distinct, nontrivial bipartitions is given by $\sum_{n_0=1}^{L/2-1} \binom{L}{n_0} + \frac{1}{2} \binom{L}{L/2} = 2^{L-1} - 1$. Bipartitions that can be mapped onto one another via translation or parity operation are considered symmetry-equivalent, as they yield identical EE values upon averaging. We therefore only need to consider a reduced set of representative bipartitions. We denote the number of such representative bipartitions with chain length L and a fixed subsystem size n_0 as $N(L, n_0)$.

Our multi-bipartition entanglement tomography is based on the geometric characterization of a bipartition via its crossed-bond vector $(n_1, n_2, \dots, n_{L/2-1})$. While symmetry-equivalent bipartitions are guaranteed to have identical crossed-bond vectors, having the same crossed-bond vector does not necessarily imply that two bipartitions are symmetry-equivalent. In fact, two bipartitions that are inequivalent under symmetry operations can accidentally possess the same crossed-bond vector.

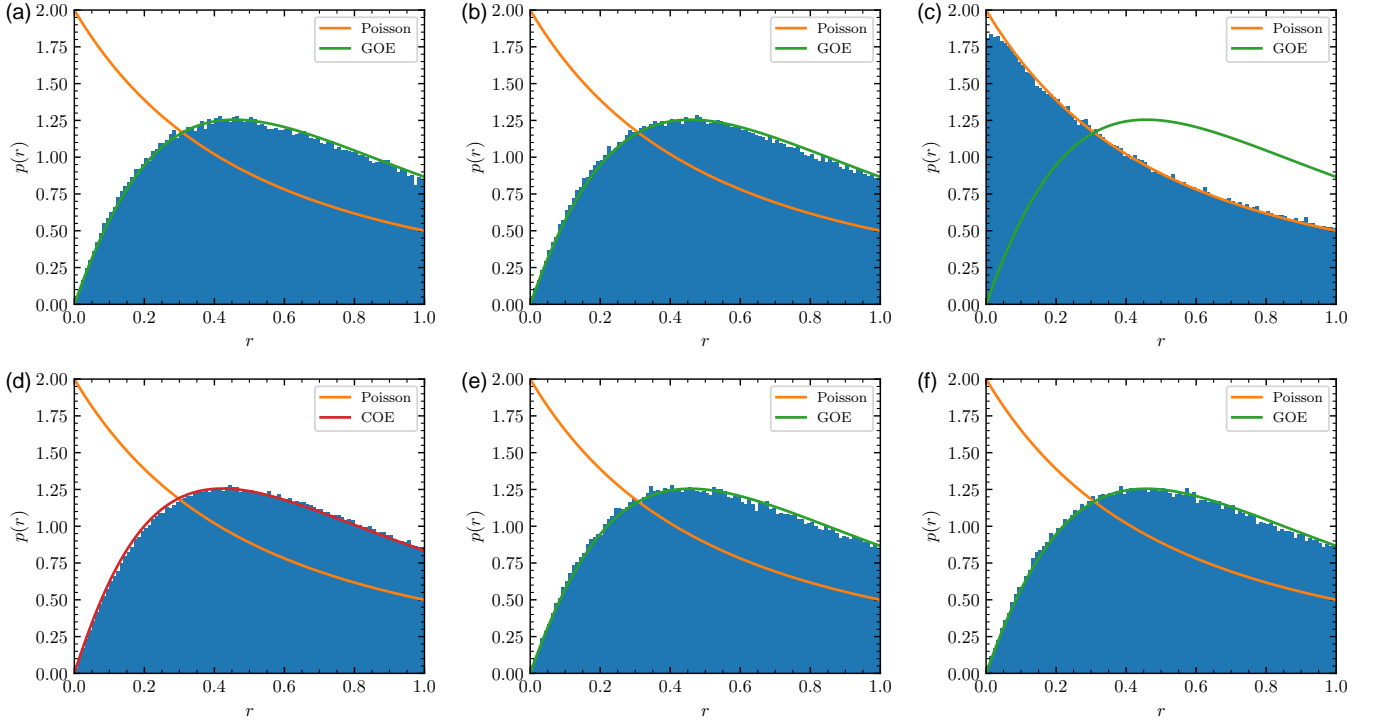


FIG. S3. Level spacing ratio distributions $p(r)$ of various operators. For comparison, the theoretical predictions are overlaid as solid lines. Subplots (a-d) show the results within the half-filling sector of $\hat{H}_{\text{NN}}(W = 0.5)$, \hat{H}_{NNNN} , $\hat{H}_{\text{NN}}(W = 5.0)$ and \hat{F} for a system size of $L = 16$. An additional result within the half-filling sector of $\hat{H}_{\text{NN}}(W = 0.5)$ for a smaller system size of $L = 12$ is shown in (f) as we consider this size for a dynamics governed by $\hat{H}_{\text{NN}}(W = 0.5)$. Subplot (e) show the result in the whole Hilbert space of \hat{H}_{MF} for $L = 12$. Each histogram in (a-d) is compiled from 100 independent samples with disorder realizations of corresponding strength and these numbers of samples in (e,f) are respectively 200 and 1000. (a) The NN thermal case for $\hat{H}_{\text{NN}}(W = 0.5)$. $L = 16$. $\bar{r} \approx 0.531$. (b) The NNN thermal case for \hat{H}_{NNNN} . $\bar{r} \approx 0.530$. (c) The MBL case for $\hat{H}_{\text{NN}}(W = 5.0)$. $\bar{r} \approx 0.390$. (d) The Floquet thermal case for $\hat{F} = e^{-iT_0 \hat{H}_0} e^{-iT_1 \hat{H}_1}$. $\bar{r} \approx 0.531$. (e) The mixed-field thermal case for \hat{H}_{MF} . $\bar{r} \approx 0.531$. (f) The NN thermal case for $\hat{H}_{\text{NN}}(W = 0.5)$. $L = 12$. $\bar{r} \approx 0.531$.

Notably, our numerical results indicate that such symmetry-inequivalent bipartitions, even when sharing an identical crossed-bond vector, can yield slightly different average EE values. This nontrivial difference means that each of the $N(L, n_0)$ representative bipartitions constitutes a distinct data point $(n_1, n_2, \dots, n_{L/2-1}, S)$ for our fitting framework. Therefore, for each fixed subsystem size n_0 with chain length L , the fit is performed on a dataset of $N(L, n_0)$ samples.

TABLE I. For a spin chain with PBC and length $L = 12$ or 16 , this table lists the number of symmetry-inequivalent representative bipartitions, $N(L, n_0)$, and the number of unique crossed-bond geometries, $M(L, n_0)$, for each subsystem size n_0 .

n_0	1	2	3	4	5	6	7	8
$N(16, n_0)$	1	8	21	72	147	280	375	257
$M(16, n_0)$	1	8	21	70	137	246	327	254
$N(12, n_0)$	1	6	12	29	38	35		
$M(12, n_0)$	1	6	12	28	35	35		

To assess the diversity of our independent variables, we also count the number of *unique* crossed-bond vectors with fixed subsystem size, denoted by $M(L, n_0)$. This quantity represents the number of distinct locations in the predictor space of our regression. By definition, $M(L, n_0) \leq N(L, n_0)$. As detailed in Table I, the values of $M(L, n_0)$ are only marginally smaller than those of $N(L, n_0)$ for the cases we considered in this paper. This confirms that the geometric configurations sampled are not highly degenerate and are well-distributed throughout the predictor space (in fact, for the situations listed in Table I, the maximum degeneracy does not exceed 3), thus ensuring the reliability of our fitting procedure.

IV. MORE RESULTS ABOUT MUTUAL INFORMATION

To contextualize the hierarchy of entanglement bond tensions $\{\omega_j\}$ discussed in the main text, this section provides a systematic comparison of the saturated mutual information $\{I_j\}$ across various thermal dynamics (Fig. S4). As observed with multi-bipartition entanglement tomography, the RQC and Floquet dynamics perfectly reproduce the Haar measure average. In contrast, the two Hamiltonian dynamics exhibit short-range mutual information, specifically at distances where direct spin interactions occur, that is significantly higher than at longer distances. These trends in mutual information closely mirror the results obtained for the entanglement bond tensions across all dynamical protocols.

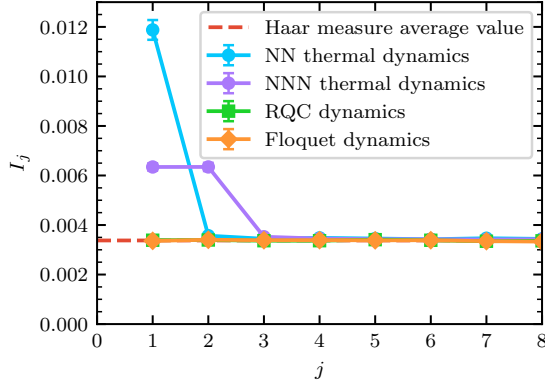


FIG. S4. Saturated mutual informations $\{I_j\}$ of various thermal dynamics for $L = 16$. Results are shown at evolution time $t = 1000.0$ for NN and NNN thermal dynamics, a circuit depth of 2000 for RQC, and after 100 periods for Floquet dynamics. All data are averaged over 1000 random samples.

V. DETAILED ANALYSIS OF FITTING QUALITY AND MORE FITTING RESULTS

This section provides a systematic analysis of the linear fitting results derived from our multi-bipartition entanglement tomography. To demonstrate the generality of our findings, we present results not only for the equal-sized bipartitions ($n_0 = L/2$) discussed in the main text, but also for several cases of unequal bipartitions ($n_0 < L/2$). We focus on relatively large values of n_0 as they involve a richer set of crossed-bond geometries and have smaller finite size effect. For each dynamical protocol, we select representative time points (or evolution depths/periods) to illustrate the entanglement bond tensions $\{\omega_j\}$ at different stages of the evolution. The following figures visualize the results in different protocols, offering clear evidence for the robustness of the bond entanglement tension hierarchy and the bond-additive law discussed in the main text.

All the data of EE used for fitting are averaged over 1000 random samples. Each figure is organized into a three-column format to offer a comprehensive view of the fitting quality and the underlying physical data: The first column shows the extracted entanglement bond tensions $\{\omega_j\}$ as a function of the bond order j . This reveals the geometric structure of entanglement. The second column shows raw distribution of the EE S as a function of the number of NN crossed bonds, n_1 . This visualizes the raw data's structure. The third column shows a direct comparison between the actual measured EE values (S) and the values predicted by our bond-additive model (S_{fitted}). The dashed red line represents the ideal case $S = S_{\text{fitted}}$. The tight clustering of data points around this line visually confirms the extremely high quality and predictive power of our multi-bipartition entanglement tomography. Fig. S5 to Fig. S7 are the case of NN thermal dynamics. Fig. S8 to Fig. S10 are the case of NNN thermal dynamics. Fig. S11 to Fig. S13 are the case of MBL dynamics. Fig. S14 to Fig. S16 are the case of mixed-field dynamics. Fig. S17 to Fig. S19 are the case of dynamics governed by $\hat{H}_{\text{NN}}(W = 0.5)$ starting from random product state without charge $U(1)$ conservation, defined in Eq. (S7). Fig. S20 and Fig. S21 are the case of RQC dynamics. Fig. S22 and Fig. S23 are the case of Floquet dynamics.

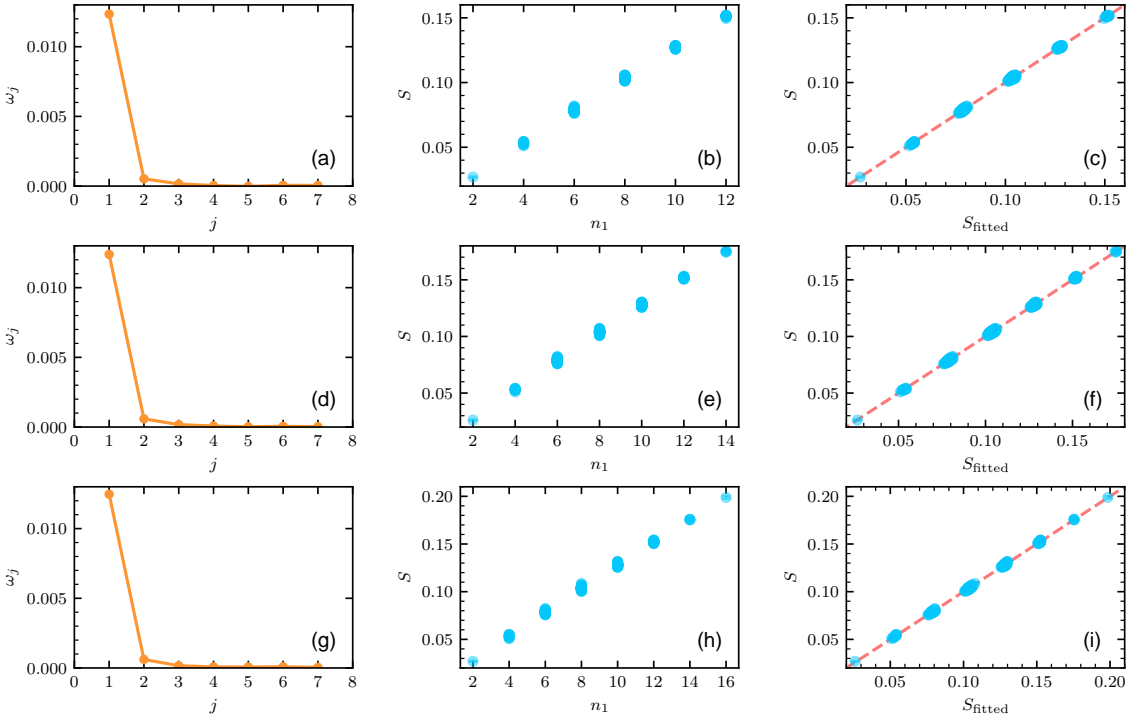


FIG. S5. Results of NN thermal dynamics for $L = 16$. Evolution time $t = 0.1$. (a-c) $n_0 = 6$, $R^2 \approx 0.9994$. (d-f) $n_0 = 7$, $R^2 \approx 0.9993$. (g-i) $n_0 = 8$, $R^2 \approx 0.9993$.

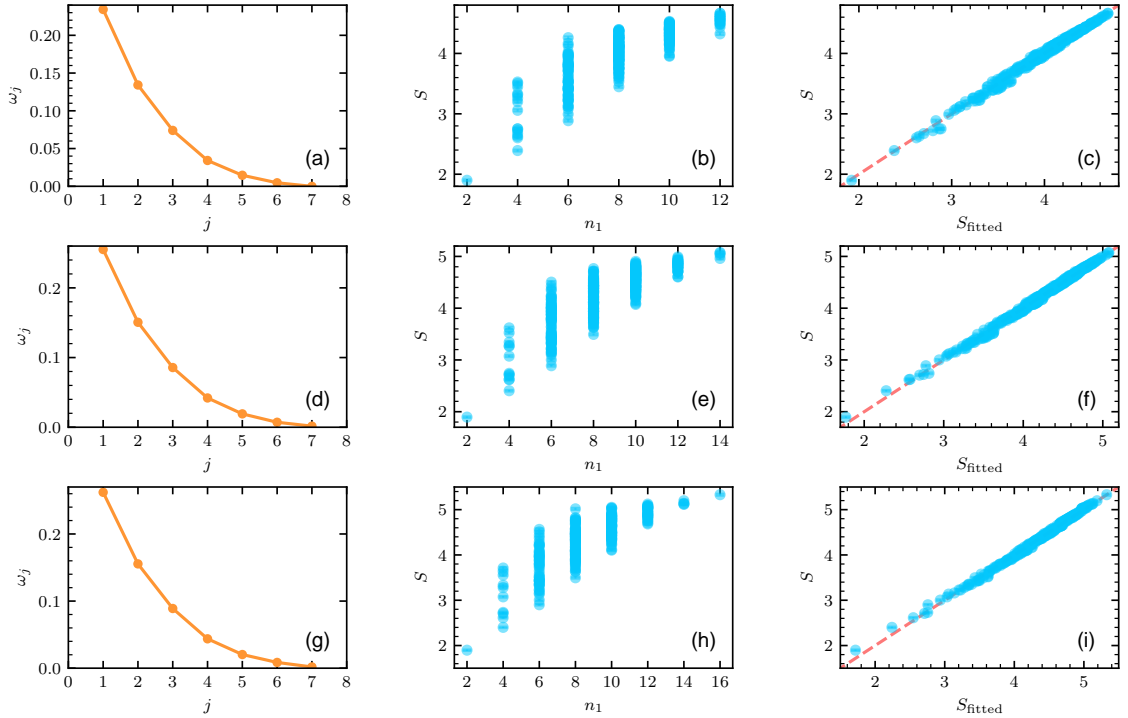


FIG. S6. Results of NN thermal dynamics for $L = 16$. Evolution time $t = 2.0$. (a-c) $n_0 = 6$, $R^2 \approx 0.9933$. (d-f) $n_0 = 7$, $R^2 \approx 0.9957$. (g-i) $n_0 = 8$, $R^2 \approx 0.9959$.

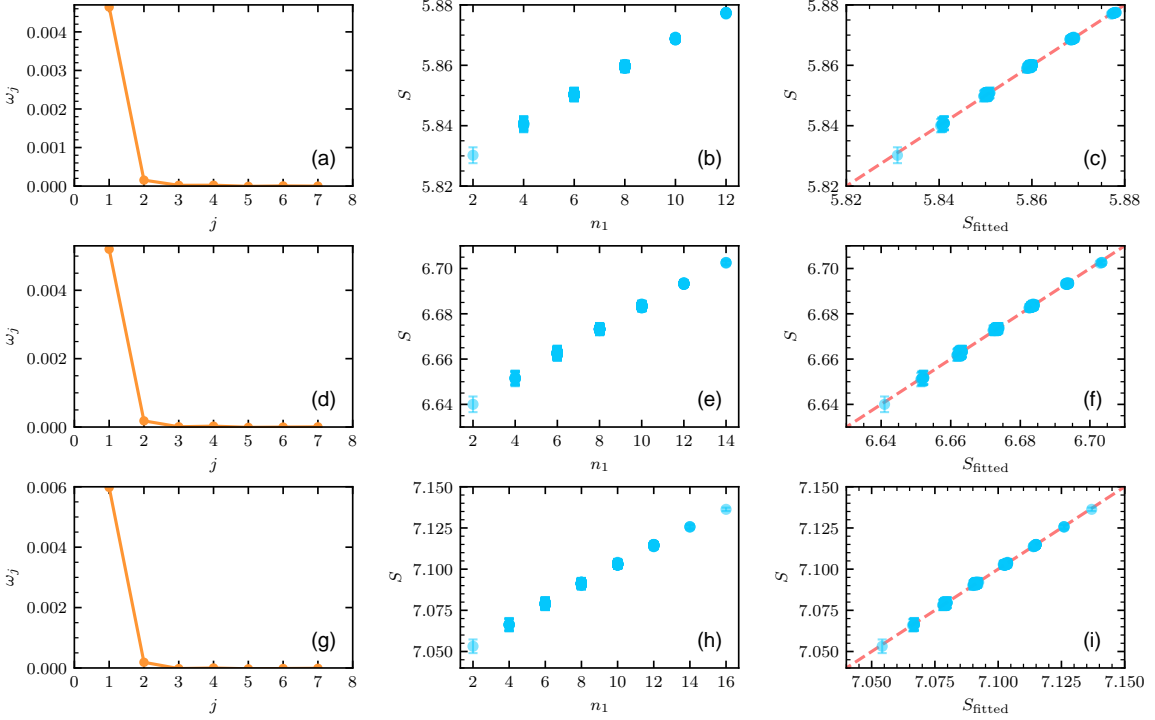


FIG. S7. Results of NN thermal dynamics for $L = 16$. Evolution time $t = 1000.0$. (a-c) $n_0 = 6$, $R^2 \approx 0.9994$. (d-f) $n_0 = 7$, $R^2 \approx 0.9994$. (g-i) $n_0 = 8$, $R^2 \approx 0.9995$.

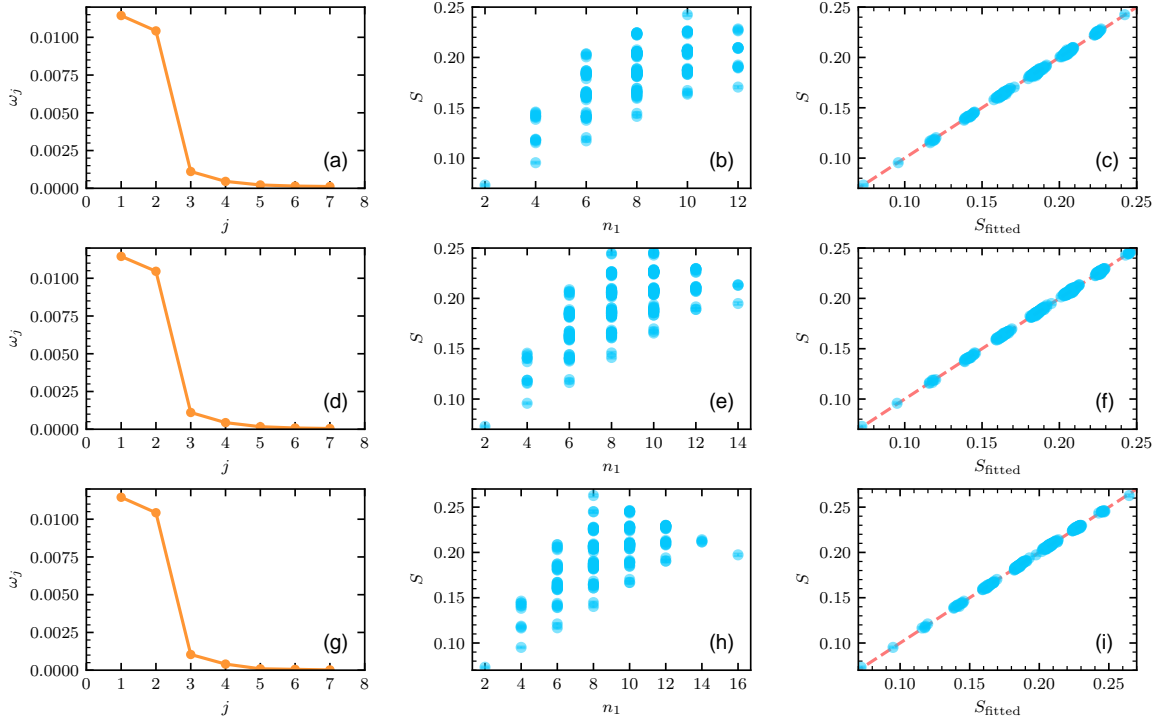


FIG. S8. Results of NNN thermal dynamics for $L = 16$. Evolution time $t = 0.1$. (a-c) $n_0 = 6$, $R^2 \approx 0.9989$. (d-f) $n_0 = 7$, $R^2 \approx 0.9991$. (g-i) $n_0 = 8$, $R^2 \approx 0.9992$.

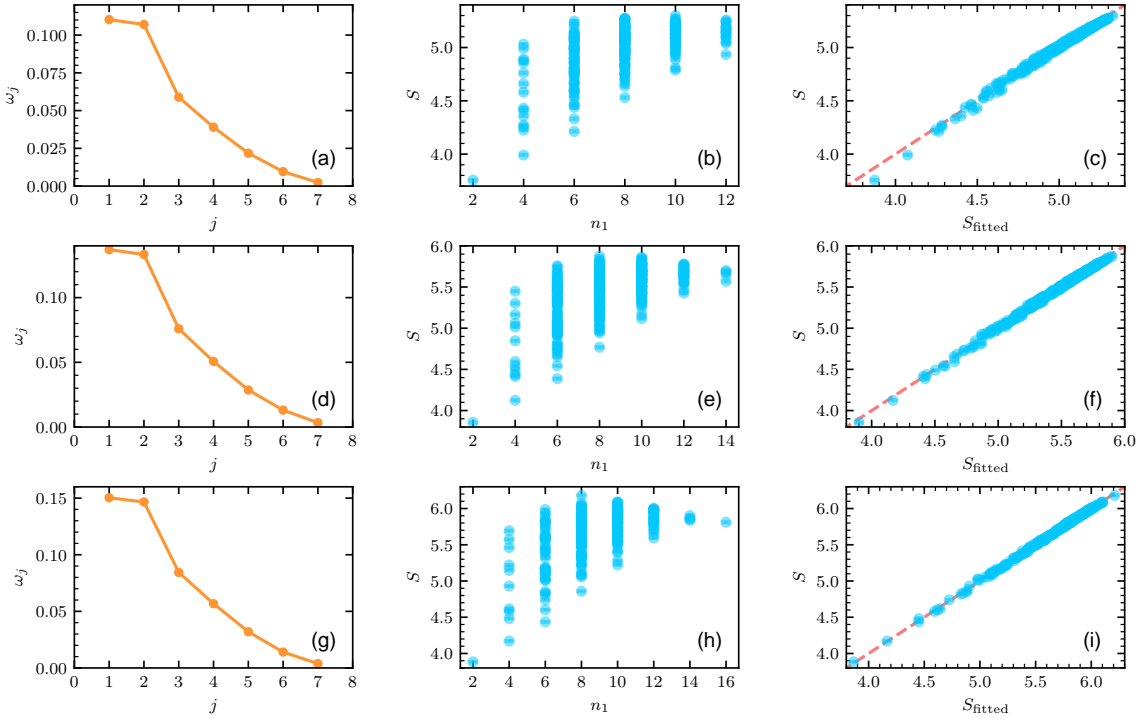


FIG. S9. Results of NNN thermal dynamics for $L = 16$. Evolution time $t = 2.0$. (a-c) $n_0 = 6$, $R^2 \approx 0.9923$. (d-f) $n_0 = 7$, $R^2 \approx 0.9974$. (g-i) $n_0 = 8$, $R^2 \approx 0.9989$.

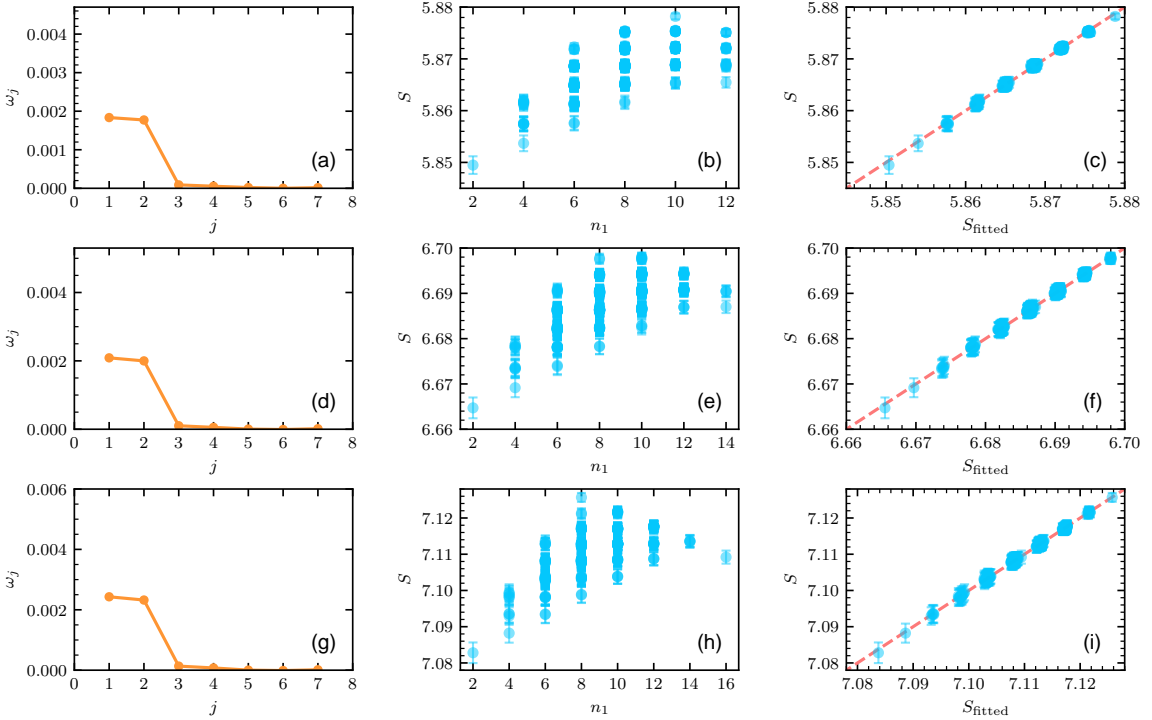


FIG. S10. Results of NNN thermal dynamics for $L = 16$. Evolution time $t = 1000.0$. (a-c) $n_0 = 6$, $R^2 \approx 0.9979$. (d-f) $n_0 = 7$, $R^2 \approx 0.9982$. (g-i) $n_0 = 8$, $R^2 \approx 0.9986$.

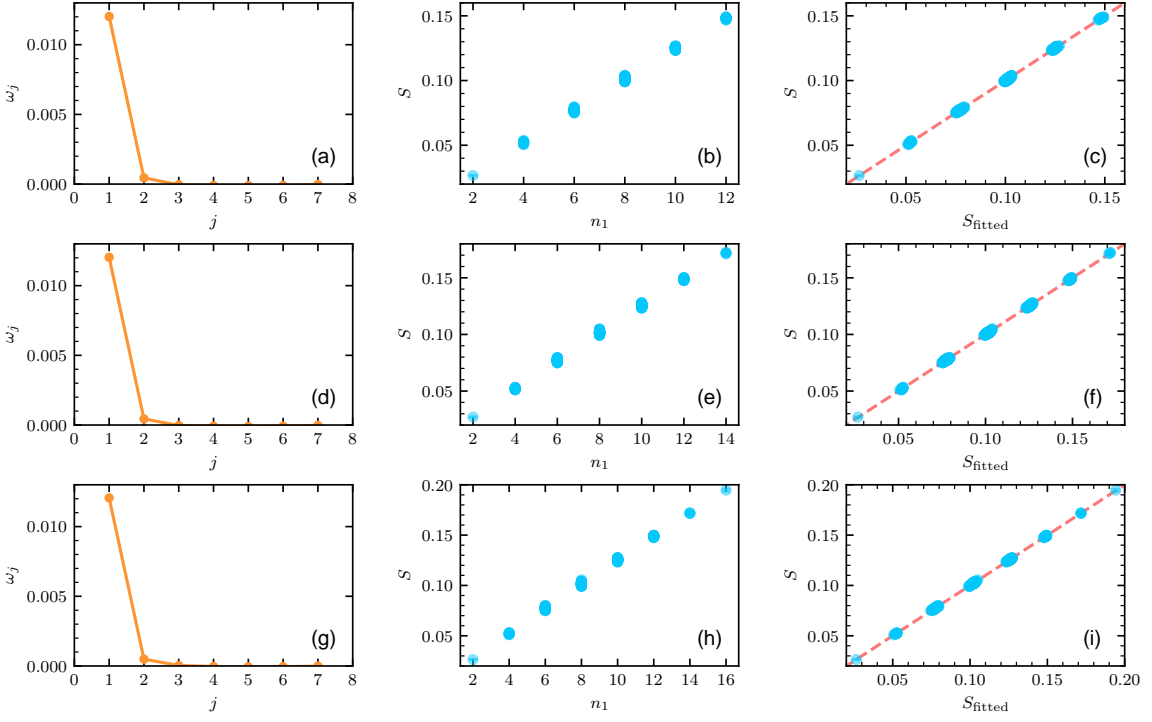


FIG. S11. Results of MBL dynamics for $L = 16$. Evolution time $t = 0.1$. (a-c) $n_0 = 6$, $R^2 \approx 0.9996$. (d-f) $n_0 = 7$, $R^2 \approx 0.9997$. (g-i) $n_0 = 8$, $R^2 \approx 0.9998$.

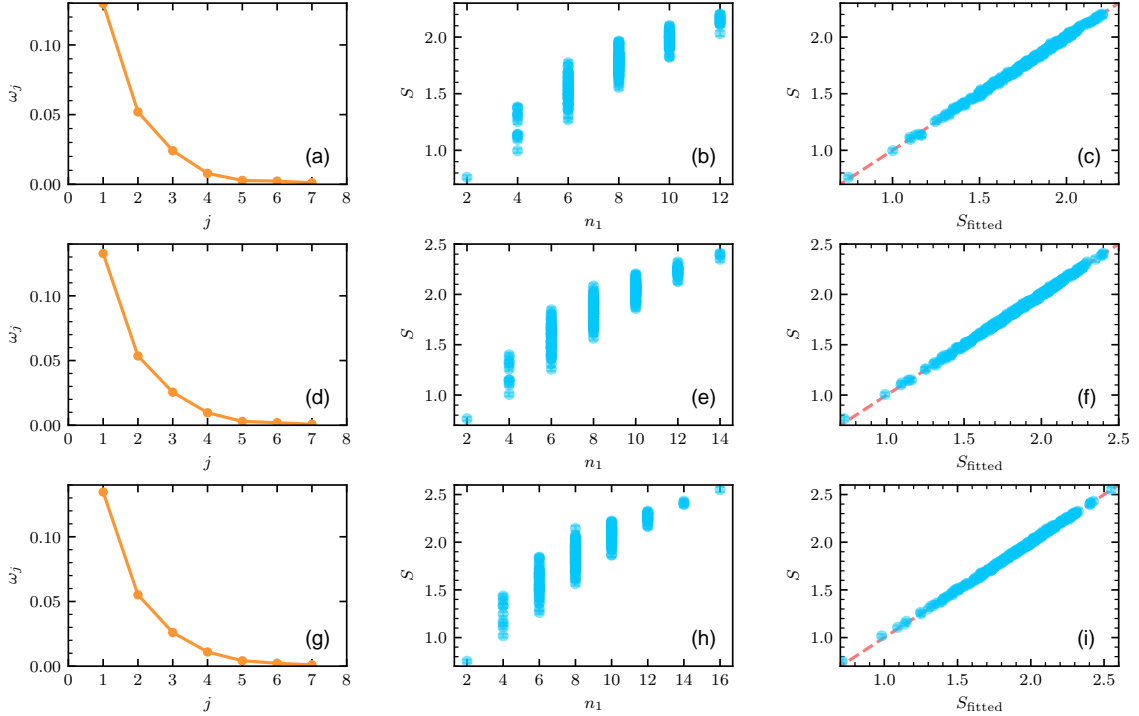


FIG. S12. Results of MBL dynamics for $L = 16$. Evolution time $t = 10.0$. (a-c) $n_0 = 6$, $R^2 \approx 0.9976$. (d-f) $n_0 = 7$, $R^2 \approx 0.9981$. (g-i) $n_0 = 8$, $R^2 \approx 0.9984$.

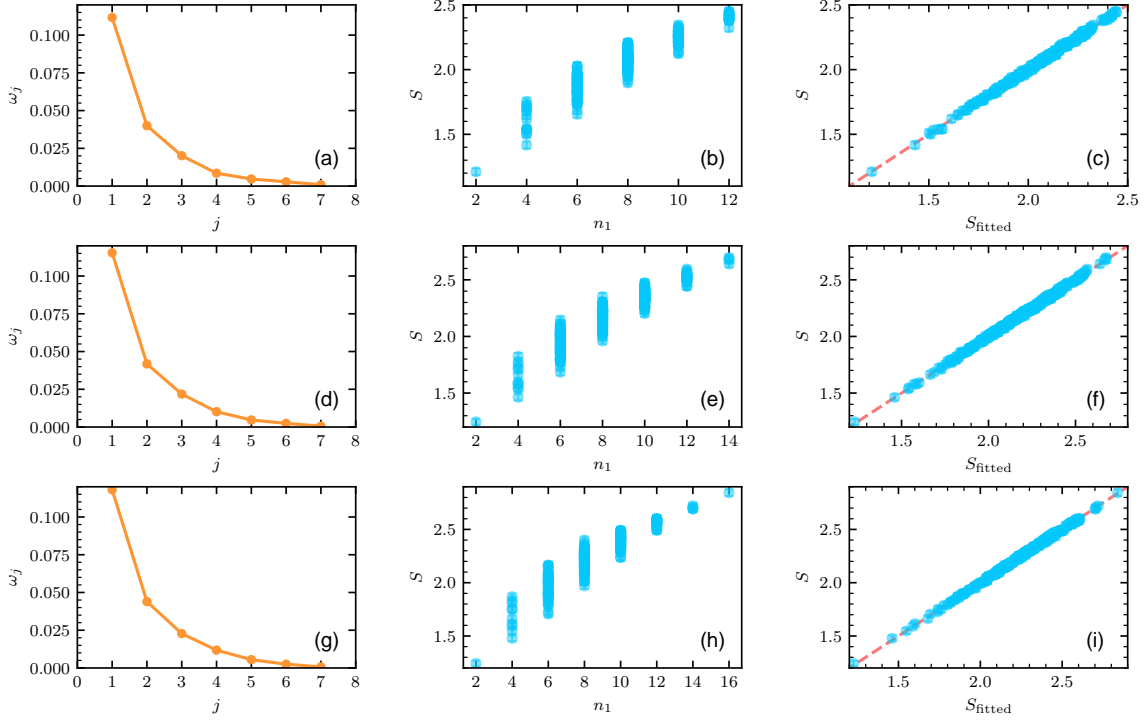


FIG. S13. Results of MBL dynamics for $L = 16$. Evolution time $t = 1000.0$. (a-c) $n_0 = 6$, $R^2 \approx 0.9972$. (d-f) $n_0 = 7$, $R^2 \approx 0.9976$. (g-i) $n_0 = 8$, $R^2 \approx 0.9981$.

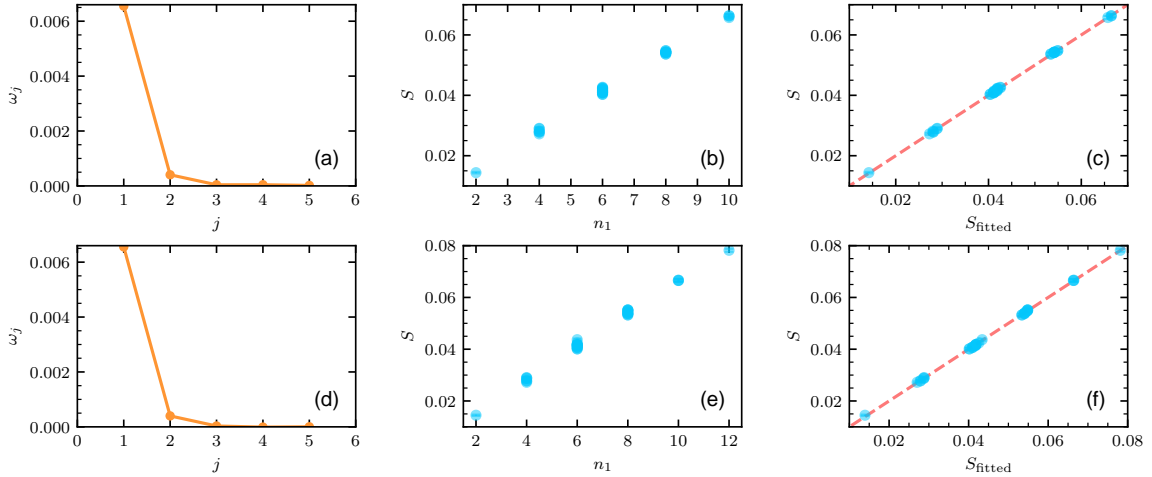


FIG. S14. Results of mixed-field dynamics for $L = 12$. Evolution time $t = 0.1$. (a-c) $n_0 = 5$, $R^2 \approx 0.9997$. (d-f) $n_0 = 6$, $R^2 \approx 0.9997$.

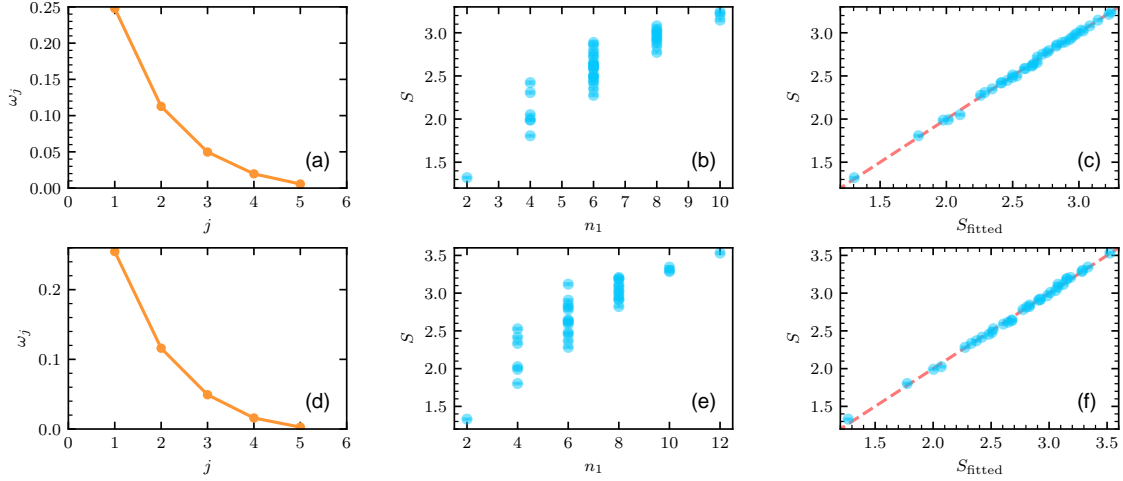


FIG. S15. Results of mixed-field dynamics for $L = 12$. Evolution time $t = 2.0$. (a-c) $n_0 = 5$, $R^2 \approx 0.9978$. (d-f) $n_0 = 6$, $R^2 \approx 0.9975$.

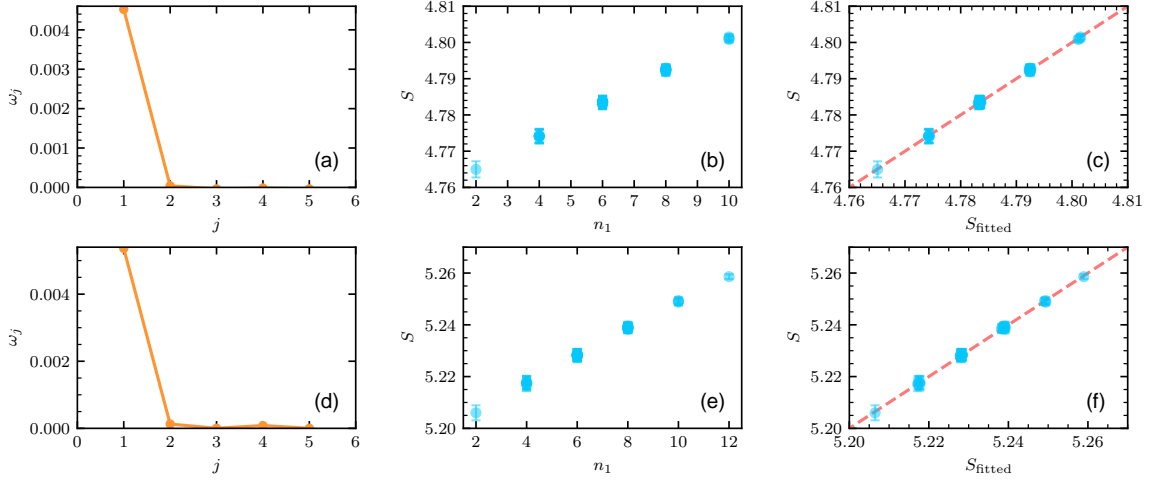


FIG. S16. Results of mixed-field dynamics for $L = 12$. Evolution time $t = 1000.0$. (a-c) $n_0 = 5$, $R^2 \approx 0.9991$. (d-f) $n_0 = 6$, $R^2 \approx 0.9990$.

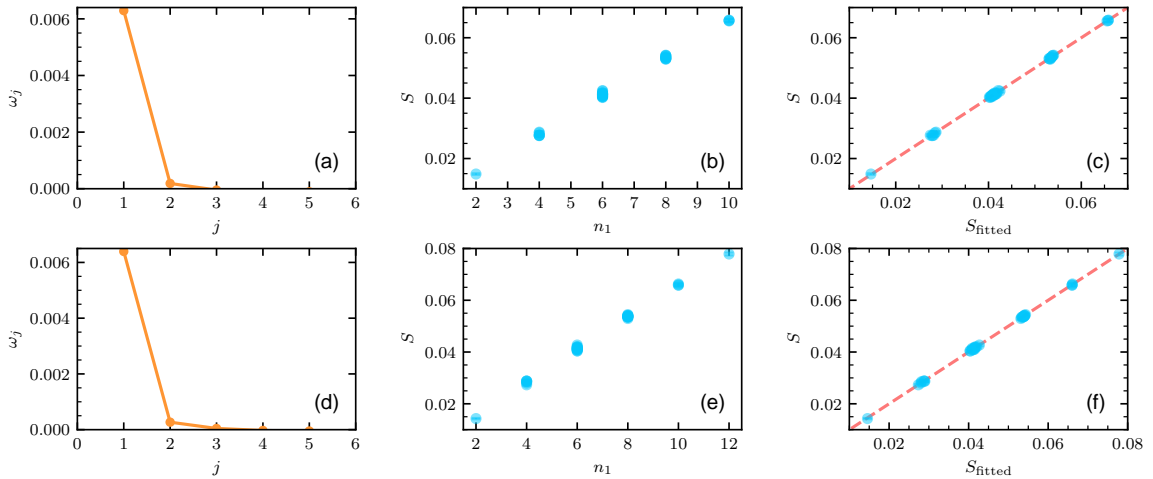


FIG. S17. Results of dynamics governed by $\hat{H}_{\text{NN}}(W = 0.5)$ starting from random product state for $L = 12$. Evolution time $t = 0.1$. (a-c) $n_0 = 5$, $R^2 \approx 0.9996$. (d-f) $n_0 = 6$, $R^2 \approx 0.9998$.

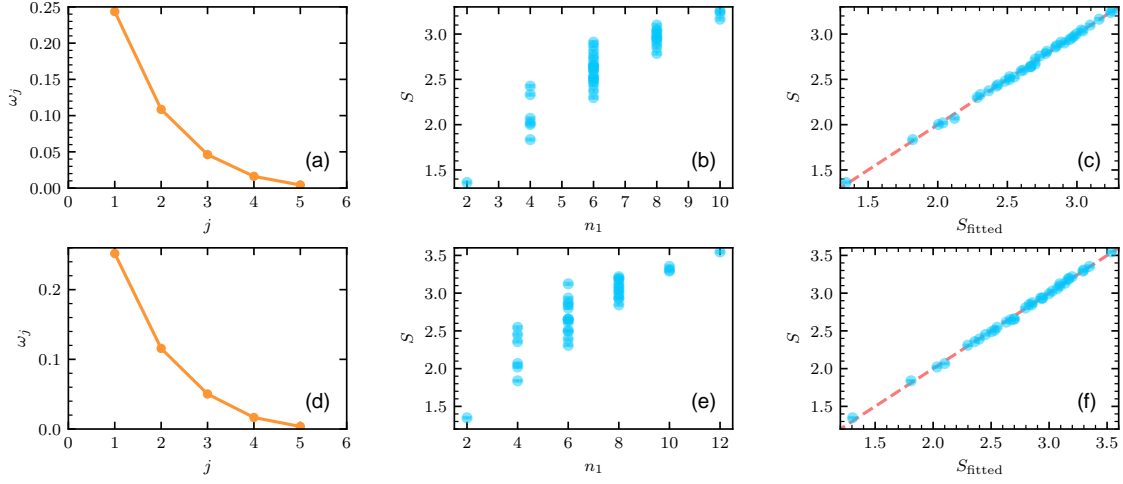


FIG. S18. Results of dynamics governed by $\hat{H}_{\text{NN}}(W = 0.5)$ starting from random product state for $L = 12$. Evolution time $t = 2.0$. (a-c) $n_0 = 5$, $R^2 \approx 0.9980$. (d-f) $n_0 = 6$, $R^2 \approx 0.9983$.

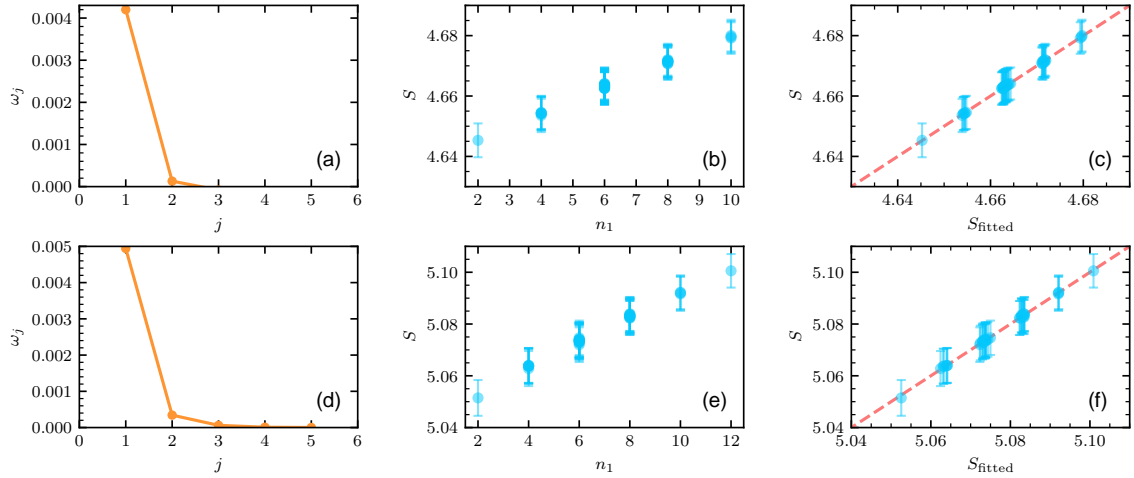


FIG. S19. Results of dynamics governed by $\hat{H}_{\text{NN}}(W = 0.5)$ starting from random product state for $L = 12$. Evolution time $t = 1000.0$. (a-c) $n_0 = 5$, $R^2 \approx 0.9991$. (d-f) $n_0 = 6$, $R^2 \approx 0.9986$.

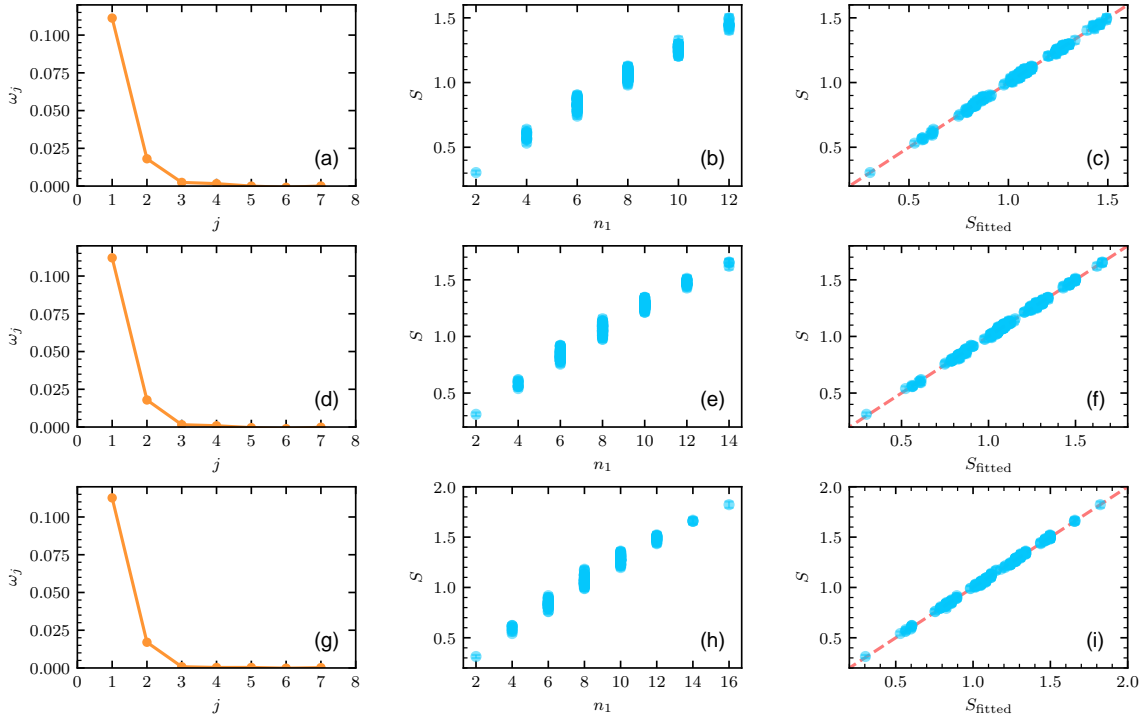


FIG. S20. Results of RQC dynamics for $L = 16$. Evolution depth is 5. (a-c) $n_0 = 6$, $R^2 \approx 0.9975$. (d-f) $n_0 = 7$, $R^2 \approx 0.9975$. (g-i) $n_0 = 8$, $R^2 \approx 0.9978$.

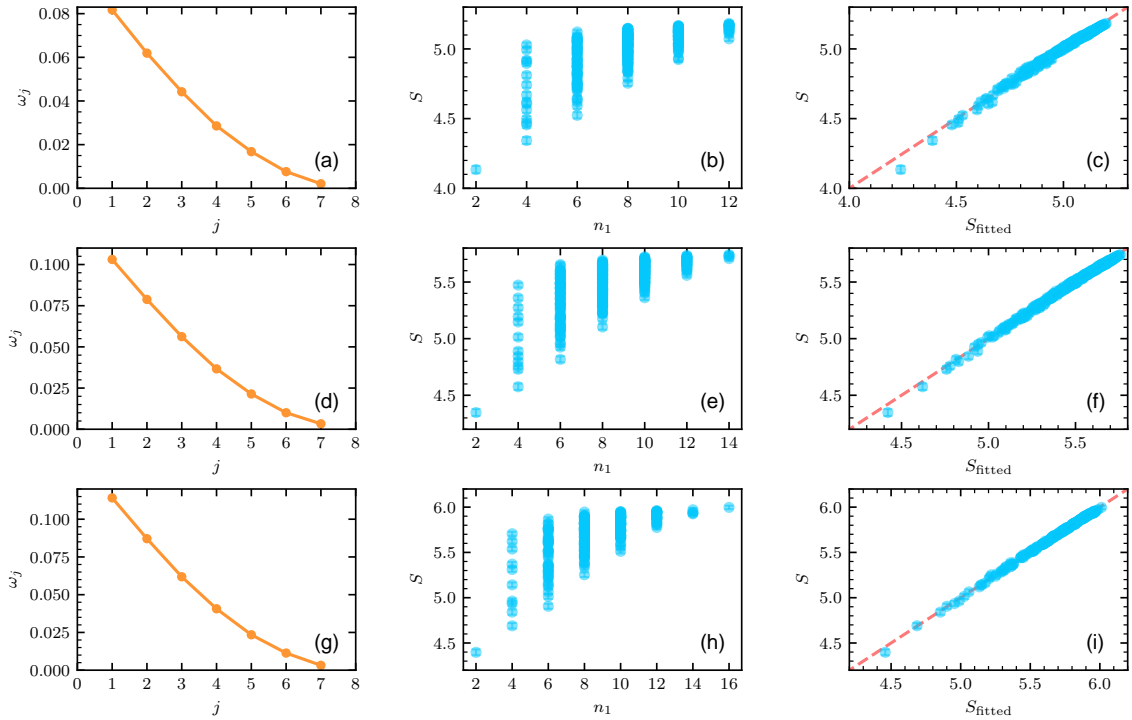


FIG. S21. Results of RQC dynamics for $L = 16$. Evolution depth is 100. (a-c) $n_0 = 6$, $R^2 \approx 0.9919$. (d-f) $n_0 = 7$, $R^2 \approx 0.9968$. (g-i) $n_0 = 8$, $R^2 \approx 0.9986$.

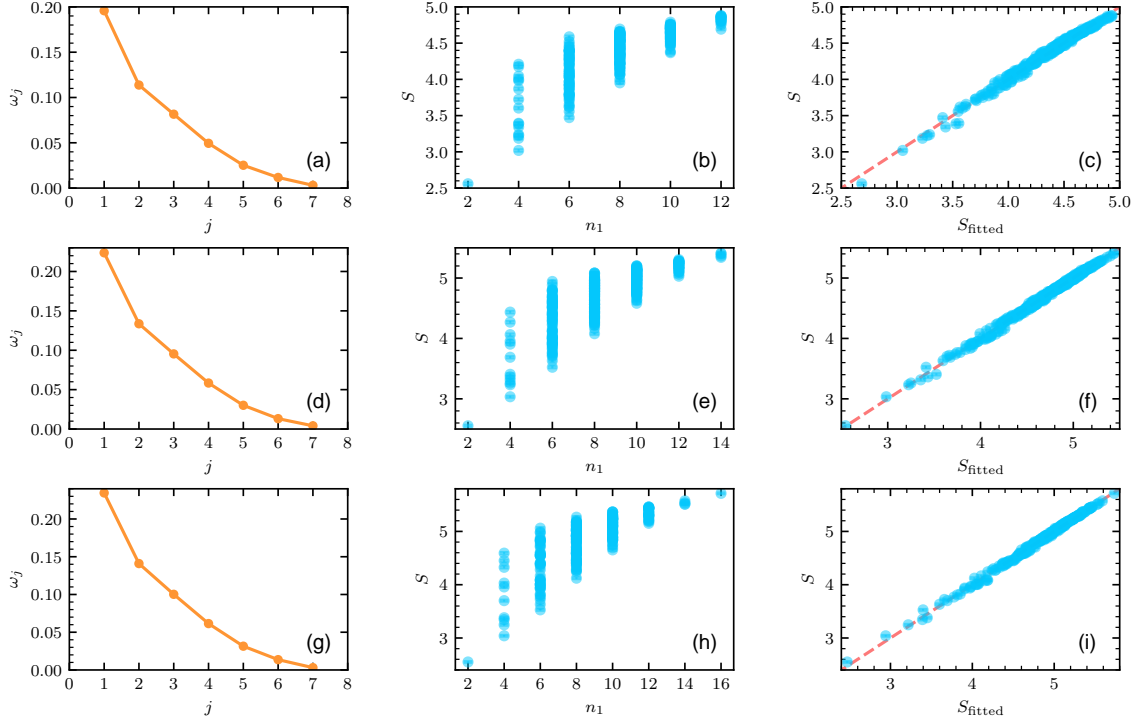


FIG. S22. Results of Floquet dynamics for $L = 16$. The period number of evolution is 1. (a-c) $n_0 = 6$, $R^2 \approx 0.9899$. (d-f) $n_0 = 7$, $R^2 \approx 0.9955$. (g-i) $n_0 = 8$, $R^2 \approx 0.9964$.

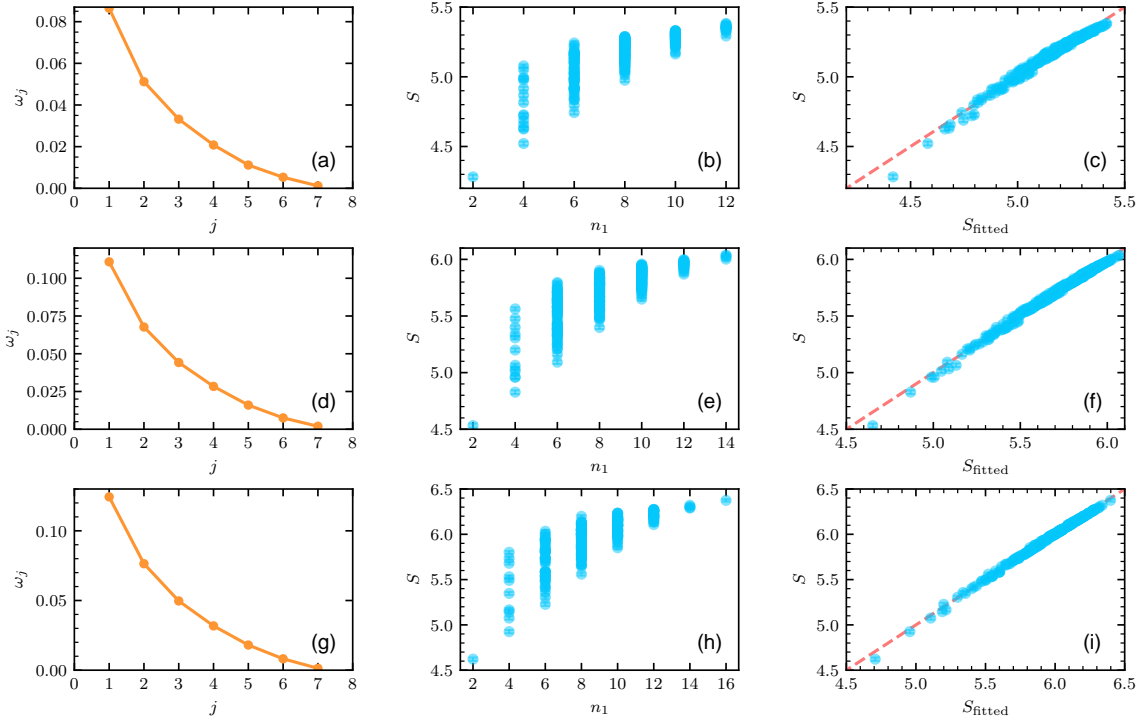


FIG. S23. Results of Floquet dynamics for $L = 16$. The period number of evolution is 3. (a-c) $n_0 = 6$, $R^2 \approx 0.9836$. (d-f) $n_0 = 7$, $R^2 \approx 0.9942$. (g-i) $n_0 = 8$, $R^2 \approx 0.9977$.